ADVANCED ENERGY MATERIALS
www.advenergymat.de

Recent Progress and Perspective of Advanced High-Energy Co-Less Ni-Rich Cathodes for Li-Ion Batteries: Yesterday, Today, and Tomorrow

Ji Ung Choi, Natalia Voronina, Yang-Kook Sun, and Seung-Taek Myung**

With the ever-increasing requirement for high-energy density lithium-ion batteries (LIBs) to drive pure/hybrid electric vehicles (EVs), considerable attention has been paid to the development of cathode materials with high energy densities because they ultimately determine the energy density of LIBs. Notably, the cost of cathode materials is still the main obstacle hindering the extensive application of EVs, with the cost accounting for 40% of the total cost of fabricating LIBs. Therefore, enhancing the energy density and simultaneously decreasing the cost of LIBs are essential for the success of EV/hybrid EV industries. Among the existing commercial cathodes, Ni-rich layered cathodes are widely employed because of their high energy density, relatively good rate capability, and reasonable cycling performance. Ni-rich layered cathodes containing Co are now being reconsidered due to the increasing price of Co, which is much higher than that of Ni and Mn. In this report, the recent developments and strategies in the improvement of the stabilities of the bulk and surface for Co-less Ni-rich layered cathode materials are reviewed.

1. Introduction

In the 1970s, Whittingham employed a TiS_2 cathode along with a lithium metal anode for lithium batteries.[1] The battery delivered a reversible capacity close to the theoretical capacity and exhibited excellent long-term cycling life. In the 1980s, Goodenough and co-workers[2] discovered that the $LiCoO_2$ cathode could extract a considerable amount of Li^+ in the range of 3–4.3 V versus Li^+/Li^0. In 1982, Yazami and Touzain reported the electrochemical activity of Li^+ ions with graphite as a solid electrolyte, which became an important basis of commercial lithium-ion batteries (LIBs).[3] In 1985, Yoshino invented a new battery comprising a $LiCoO_2$ cathode and carbonaceous anodes, which displayed a reasonable reversible capacity and significantly enhanced cyclability.[4] Subsequently, LIBs were commercialized by Sony in 1991; these exhibited enhanced gravimetric energy density and volumetric energy density compared with those of nickel–cadmium and nickel–metal hydride batteries.[5] Considering their high reversible capacity and appreciable calendar life, LIBs have been widely applied in consumer products (such as cameras and laptops) and pure/hybrid (H) electrical vehicles (EVs). According to the price chart of the elements, comprising LIBs, Co ($15.54) is more expensive than Ni, Mn, and Al, which are priced at $5.90, $1.06, and $0.77 USD LB^{-1}, respectively, the real-time price on February 6, 2020, http://www.infomine.com/investment/metal-prices/. This has motivated the search for alternative cathode materials with low cost and high capacity for popularization of EVs/HEVs that adopt LIBs as power sources (**Figure 1**a).[6] Replacing Co with other elements in the layered structure may lead to excellent cell performance. For example, Ni-rich $Li[Ni_{1-x-y}Co_xMn_y]O_2$ affords high capacities (200–250 mAh g^{-1}) and high-voltage operation (≈3.8 V vs Li^0/Li^+) as well as better chemical stability with reduced oxygen loss due to the lack of significant overlap of the $Ni^{3+/4+}$ (e_g) redox energy with the top of the O^{2-} 2p band above the $Co^{3+/4+}$ (t_{2g}) and $Mn^{3+/4+}$ (t_{2g}) bands.[7,8] However, synthesis of stoichiometric $LiNiO_2$ is difficult because of the similar ionic radii of Li^+ (0.76 Å) and Ni^{2+} (0.69 Å), i.e., Ni^{2+} can easily occupy the 3*b* lithium sites in the Li slab and form $[Li_{1-x}Ni_x]_{3a}[Ni_{1-x}]_{3b}[O_2]_{6c}$ during synthesis. The presence of Ni^{2+} in the lithium layer not only impedes facile Li^+ diffusion but also results in irreversible capacity and poor cycling life.[9] Generally, $LiNiO_2$ exhibits progressive phase transition from the first hexagonal to monoclinic (H1 to M), monoclinic to the second hexagonal (M to H2), and finally, second hexagonal to the third hexagonal (H2 to H3) phases upon deep delithiation,[10] which constrains the

Dr. J. U. Choi, Dr. N. Voronina, Prof. S.-T. Myung
Hybrid Materials Research Center
Department of Nanotechnology and Advanced Materials Engineering & Sejong Battery Institute
Sejong University
Seoul 05006, South Korea
E-mail: smyung@sejong.ac.kr
Prof. Y.-K. Sun
Department of Energy Engineering
Hanyang University
Seoul 04763, South Korea
E-mail: yksun@hanyang.ac.kr
The ORCID identification number(s) for the author(s) of this article can be found under https://doi.org/10.1002/aenm.202002027.

DOI: 10.1002/aenm.202002027

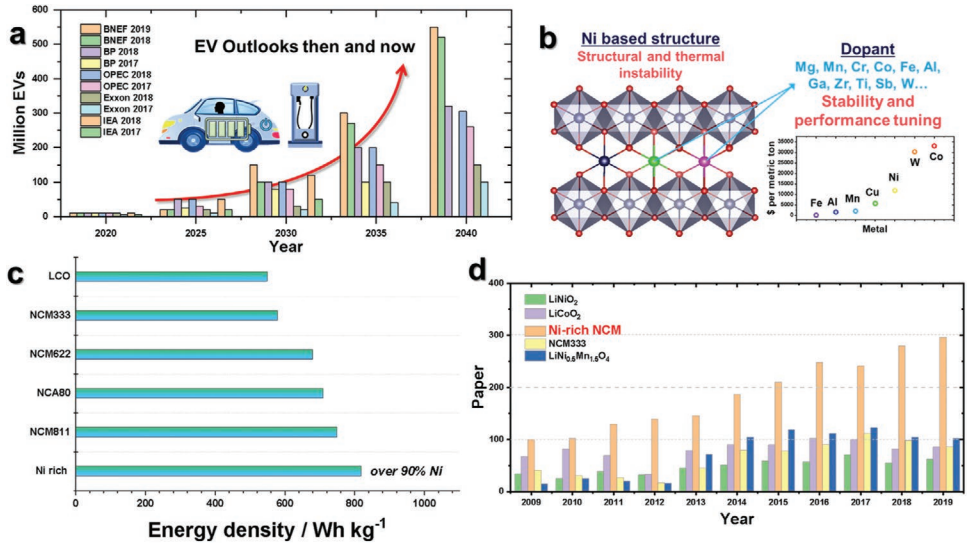

Figure 1. a) EV outlooks (then and now) estimated by BNEF, BP, OPEC, Exxon, and IEA companies (https://www.greencarcongress.com/2019/05/20190516-bnef.html). b) Basic strategies to overcome the structural and thermal instability for $LiNiO_2$ using various dopants (Mg, Mn, Cr, Co, Fe, Al, Ga, Zr, Ti, Sb, and W) with their prices in $ per metric ton. c) Energy densities of a series of commercialized Ni-based cathodes and next-generation Co-less Ni-rich cathodes for LIBs. d) Research papers focused on cathode materials for LIBs over the last 10 years (Scopus Search data).

long-term cyclability of $LiNiO_2$. This drastic variation in the *c*-axis lattice parameter is thought to be one of the factors that accelerate the rupture of active particles. Furthermore, the evolution of O_2 from the crystal lattice at a highly delithiated state threatens the thermal stability over 180 °C; simultaneously, the decomposition triggers an exothermic reaction, such that the hexagonal structure is vigorously transformed to a cubic spinel $LiNi_2O_4$, and rocksalt NiO with a significant amount of oxygen being released from the parent compound.[11] This induces structural mismatch among the hexagonal layered structure and the newly formed unwanted cubic spinel $LiNi_2O_4$ and rock salt NiO, which eventually generates microcracks within the delithiated particles.[12] The undesirable cation disordering, multistep phase transition, microcrack formation, and O_2 release result in structural degradation of $LiNiO_2$.[13] To resolve these issues, Ni in $LiNiO_2$ was partially substituted with other elements[14] such as Mg, Mn, Cr, Fe, Co, Al, Ga, Zr, Ti, Sb, and W to determine their roles in the $LiNiO_2$ structure (Figure 1b and **Table 1**). Partial substitution of Ni by Co in $LiNiO_2$ may contribute to facile electron transfer at high rates due to the overlap in density of states between the O 2p and Co 3d ($Co^{3+/4+}$) orbitals in $LiCoO_2$.[15] Furthermore, substitution of Ni by Mn in $LiNiO_2$ improves the structural stability due to the presence of electroinactive Mn^{4+} in the $Li[Ni_{1-x-y}Co_xMn_y]O_2$ (NCM) cathode.[16] As a result, the Co-less Ni-rich NCM (Ni > 90%) layered cathode is considered as the most promising cathode material due to its high discharge capacity (>200 mAh g^{-1}), high energy density (>750 Wh kg^{-1}), and improved structural stability (Figure 1c). Over the last 10 years, Ni-rich NCM layered cathodes have been intensively investigated compared with other cathode materials (Figure 1d). More importantly, Co-less Ni-rich layered NCM cathodes can be fabricated at a low cost because of the reduced Co content. Herein, we focus on the developments and challenges of Co-less Ni-rich layered oxides, including $LiNiO_2$, binary-, ternary-, and quaternary-Ni-rich $LiNiO_2$ cathodes; they are classified as "past," "present," and "future."

Table 1. Summary of the effect of dopants in $LiNiO_2$.

Dopant	Advantage	Disadvantage
Mg^{2+}	Structural stabilization (pillar effect)	Reduction of the discharge capacity (Inactive Mg^{2+})
Mn^{3+}	Structural stabilization	Poor power capability
Cr^{3+}	Structural stabilization	Reduction of the discharge capacity
Co^{3+}	Effective in decreasing cation mixing and battery performance	Expensive
Fe^{3+}	Earth abundance Low cost	Reduction of the discharge capacity Poor cyclability
Al^{3+}	Low cost Lighter atomic weight	Reduction of the discharge capacity (Inactive Al^{3+})
Ga^{3+}	Overcharge resistance	Reduction of the discharge capacity
Zr^{4+}	Structural stabilization	Reduction of the discharge capacity
Ti^{4+}	Structural stabilization	Reduction of the discharge capacity (Inactive Ti^{4+})
Sb^{5+}	Increase of operating voltage	Reduction of the discharge capacity
W^{6+}	Decreased primary particle size	Expensive

2. Co-Less Ni-Rich Cathodes of Past

2.1. $LiNiO_2$

$LiNiO_2$ adopts a phase that is isostructural with α-$NaFeO_2$, where the oxide ions form a cubic close-packed arrangement that has a rhombohedral crystal structure with the *R*-3*m* space group (**Figure 2**a).[17,18] Generally, layered cathodes are clearly divided into the transition-metal sites (3*a*) and lithium sites (3*b*), as shown in the inset of Figure 2a.[18] $LiNiO_2$ was first introduced by Dyer et al. in the early 1950s[19] and is considered an attractive cathode that is relatively cost-effective compared

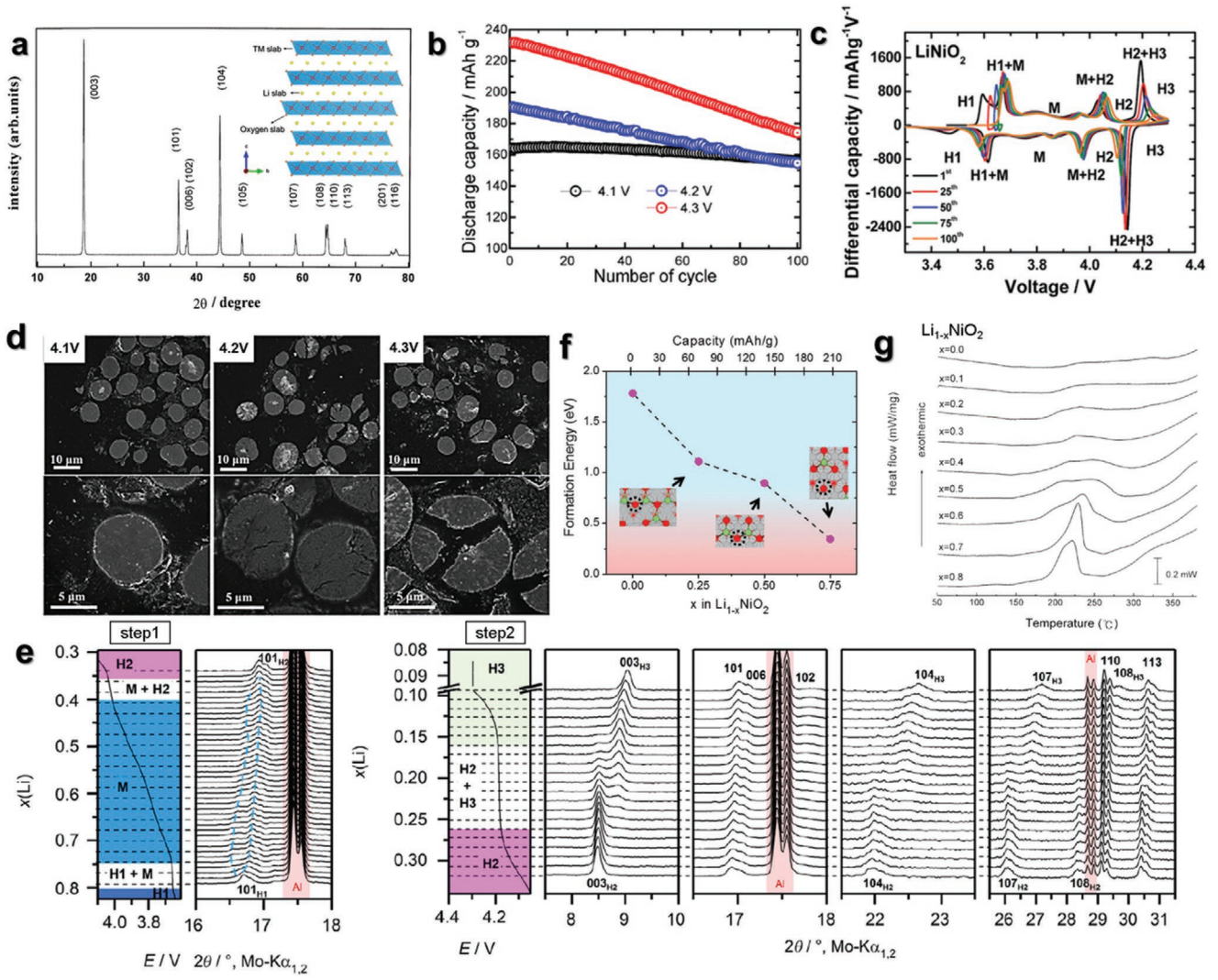

Figure 2. a) X-ray diffraction pattern of $LiNiO_2$ powders calcined at 750 °C. Reproduced with permission.[18] Copyright 1999, Elsevier. Electrochemical performance of LNO cathodes at different upper cutoff voltages from 2032 coin-type half-cells with Li as the anode. b) Cycling performance at 0.5C (90 mA g^{-1}). Reproduced with permission.[25] Copyright 2017, American Chemical Society. c) $dQ\ dV^{-1}$ profile as a function of the number of cycles for $LiNiO_2$ (H = hexagonal and M = monoclinic structures). Reproduced with permission.[26] Copyright 2018, Royal Society of Chemistry. d) Cross-sectional SEM images of the initial charge-ended LNO cathode at 4.1, 4.2, and 4.3 V at different magnifications. Reproduced with permission.[25] Copyright 2017, American Chemical Society. e) Selected diffraction patterns showing the splitting of the (101) reflection in the monoclinic phase region and selected diffraction patterns of the H2–H3 transformation region. Reproduced with permission.[28] Copyright 2019, John Wiley and Sons. f) Oxygen vacancy formation energy during delithiation of $LiNiO_2$. Reproduced with permission.[29] Copyright 2018, John Wiley and Sons. g) DSC results for $Li_{1-x}NiO_2$ composites in air atmosphere at a heating rate of 5 °C min^{-1}. Reproduced with permission.[30] Copyright 2001, Elsevier.

with $LiCoO_2$, affording a high capacity (200–250 mAh g^{-1}) and high-voltage operation (≈3.8 V vs Li^0/Li^+). However, the ideal stoichiometric $LiNiO_2$ with a Li:Ni ratio of 1:1 is difficult to synthesize because of the formation of a Li-deficient phase ($Li_{1-x}Ni_{1+x}O_2$), in which the presence of Ni^{2+} leads to Li^+/Ni^{2+} cation mixing during synthesis. A large portion of the cation mixing in the Li layer may result in the formation of inactive $Li_2Ni_8O_{10}$, which suppresses Li diffusion causing poor power capability.[17] The I_{003}/I_{104} peak value is a measure of the degree of Li^+/Ni^{2+} cation mixing, which was suggested by Ohzuku et al. to evaluate the relationship between the crystal structure and electrochemical performance.[20] The (003) peak indicates diffraction of the original layered structure that crystallizes in the *R*-3*m* space group, while the (104) peak arises from the layered and cubic rock salt $Ni^{2+}O$ structure.[21] An I_{003}/I_{104} value exceeding 1.2 indicates a well-formed layered structure with a small degree of Li^+/Ni^{2+} cation mixing. Many researchers have reported that the Li storage mechanism in $LiNiO_2$ involves multiphase transitions during charge–discharge, leading to structural instabilities.[7,22] According to Ohzuku[21] and Delmas and co-workers,[23] Li_xNiO_2 ($0.3 < x < 1$) is divided into four district regions in terms of various lattice parameters.[24]

Recently, Sun and co-workers reported that a $LiNiO_2$ cathode prepared via the co-precipitation method exhibited relatively high reversible capacity in various voltage ranges (Figure 2b),[25] showing increased discharge capacity from ≈180 to ≈230 mAh g^{-1} by increasing the upper cutoff voltage from

4.2 to 4.3 V. Unfortunately, $LiNiO_2$ still suffered from drastic capacity fading over 100 cycles of operation presumably because of the irreversible multiphase transition upon extensive cycling, as evidenced from the $dQ\ dV^{-1}$ curves at the cutoff voltage of 4.3 V (Figure 2c).[26] H1, M, H2, and H3 phases were reversible, while the appearance of the H3 phase was associated with the drastic variation in the *c*-axis lattice parameter that directly affects capacity fading.[10] Delmas and co-workers reported that the splitting of the (101) X-ray diffraction (XRD) peak at the highly delithiated Li_xNiO_2 state was closely associated with the presence of the NiO_2 composition that produced AB stacking faults (O1-type structure) in the O3-type structure.[27] The presence of the highly delithiated Li_xNiO_2 (*R*-3*m*) space group at the outer surface and at the inner side (*R*-3*m*) with many stacking faults was confirmed by high-resolution transmission electron microscopy (HRTEM).[25] That is, the stacking faults were ascribed to the formation of NiO_2, which leads to the degradation of the structure during cycling due to the considerable variation of the *c*-axis lattice during extensive cycling in the delithiated Li_xNiO_2, although the $LiNiO_2$ particles were undamaged by unwanted phase transition when charged to 4.1 V (Figure 2d).[25] When the particles were charged to over 4.2 V, the $LiNiO_2$ particles showed signs of damage, with the formation of internal microcracks, even during the first charge.

As is well known, the phase transition from the H2 phase to the H3 phase at a high charge state in $LiNiO_2$ induces significant structural instability.[28] When delithiated Li_xNiO_2 ($x \approx 0.26$) was charged to 4.1 V, it underwent a relatively stable phase transition from the H1 to M and M to H2 phases (Figure 2e, step 1).[28] On further charging over 4.2 V, $LiNiO_2$ underwent severe structural changes with a dramatic contraction of the *c*-axis lattice parameter upon the unstable phase transition from H2 to H3 (Figure 2e, step 2).[28] Thus, $LiNiO_2$ showed a high discharge capacity of ≈250 mAh g^{-1}, but with drastic capacity fading at the high cutoff voltage upon extensive cycling, as shown in Figure 2b.

Not only structural instability but the thermal instability of $LiNiO_2$ has also been one of the largest obstacles to their application in EVs, which demand high-voltage operation. Early studies on thermal instability of fully delithiated Li_xNiO_2 with $x < 0.5$ detected oxygen evolution at emerging temperatures of 100–200 °C, which was thermodynamically calculated by Cho and co-workers using the formation energy for the oxygen vacancy as a function of depth of charging by incrementally removing Li from $LiNiO_2$ (Figure 2f).[29] The formation energy of an oxygen vacancy for fully lithiated $LiNiO_2$ is 1.8 eV, and it decreases rapidly upon delithiation. When 75% of Li^+ is removed (at a charge capacity of 210 mAh g^{-1}) the corresponding formation energy for oxygen vacancy becomes approximately 0.35 eV. That is, the $Li_{1-x}NiO_2$ becomes considerably thermally stable without the release of significant amount of heat or oxygen vacancy, but the delithiated $Li_{1-x}NiO_2$ ($0.1 \le x \le 0.8$) showed thermal instability which indicated that the exothermic reaction further increased at approximately 220 °C with an increased degree of deintercalation (Figure 2g).[30] Therefore, as the capacity of $LiNiO_2$ of $LiNiO_2$ reaches over 200 mAh g^{-1}, the bulk oxygen evolution at emerging temperatures in the range of 100–200 °C represents a fundamental challenge of thermal instability of the Ni-rich cathode materials.

2.2. Strategies that Improved the Structural and Thermal Stabilities of $LiNiO_2$

The replacement of Ni in $LiNiO_2$ with alternative dopants such as Mg^{2+},[31] Mn^{3+},[32] Cr^{3+},[33] Co^{3+},[15,34,35] Fe^{3+},[36] Al^{3+},[37] Ga^{3+},[38] Zr^{4+},[39] Ti^{4+},[40] Sb^{5+},[41] and W^{6+}[42] could suppress the decomposition of delithiated $Li_{1-x}NiO_2$ into the unwanted cubic spinel $LiNi_2O_4$ and rock salt NiO, leading to structural deterioration by multiphase transition. In particular, the severe structural changes with drastic lattice contraction in highly delithiated Li_xNiO_2 could be resolved by the doping effect. Multiphase transition was simplified in $LiNiO_2$ with various dopants, and the drastic contraction in highly delithiated Li_xNiO_2 was strongly curtailed.

2.2.1. Improved Structural Stability

Delmas and co-workers reported that by partial introduction of Mg^{2+} into $LiNiO_2$, Mg^{2+} played the role of a pillar in the structure because Mg^{2+} replaced Li in the Li layer owing to their similar ionic radii (0.72 Å of Mg^{2+} and 0.76 Å of Li^+).[31] In addition, Ni^{2+} in the $[Li_{1-x}Ni_x]_{3a}[Ni_{1-x}]_{3b}[O_2]_{6c}$ phase can be substituted with Mg^{2+}. Therefore, the interslab space is not strongly affected by severe shrinkage of the structure upon Li^+ deintercalation due to the pillar effect provided by the electrochemically inactive Mg^{2+}.[31] This explains why Mg^{2+}-doped $LiNiO_2$ phases reported by Shakkthivel and co-workers exhibited good cyclability despite the further reduction of the discharge capacity with increasing Mg content in $LiNiO_2$ (**Figure 3**a).[43] Partial substitution of Ni by Mn in $LiNiO_2$ is worthwhile due to the low cost of Mn and similarity between the ionic radii of Ni^{3+} (0.6 Å) and Mn^{3+} (0.65 Å).[32] Although the $LiNi_{1-x}Mn_xO_2$ ($0.1 \le x \le 0.5$) cathode delivers relatively lower specific capacity due to inert Mn^{4+}, this cathode shows better capacity retention with improved structural stability than $LiNiO_2$.[44,45] This is associated with the suppression of the phase transition from H2 to H3, as confirmed by analysis of the samples with increasing Mn content at a voltage of 4.2 V (Figure 3b).[32] Thus, the cycling stability improved with increasing Mn content in the $LiNi_{1-x}Mn_xO_2$ structure. However, a higher Mn content in layered $LiNi_{1-x}Mn_xO_2$ led to poor power capability.[32] $LiNi_{0.9}Mn_{0.1}O_2$ delivered a high discharge capacity of ≈160 mAh g^{-1} at 10C, which corresponds to a retention of 76% with respect to the discharge capacity of ≈201 mAh g^{-1} obtained at 0.1C. In contrast, the discharge capacity of $LiNi_{0.5}Mn_{0.5}O_2$ was only ≈50 mAh g^{-1} at 10C, which corresponds to a retention of 31% with respect to the discharge capacity of ≈160 mAh g^{-1} at 0.1C. Hence, the partial substitution of Ni by Mn in $LiNiO_2$ can improve the cyclability with structural stability, but the poor power capability must be ameliorated to develop energy storage systems with long cycle life at high rates.

Co addition in the $LiNiO_2$ cathode has been shown to improve the structural stability and electrochemical performance, as $Ni^{3+/4+}$ and $Co^{3+/4+}$ redox pairs exhibit similar redox behavior at high voltages. The partial substitution of Co for Ni in $LiNiO_2$ is beneficial for facile electron transfer due to the overlap of the O 2p orbital with that of the $Co^{3+/4+}$ redox pair.[8,34] Saadoune and Delmas[46] and Zhecheva and Stoyanova[47]

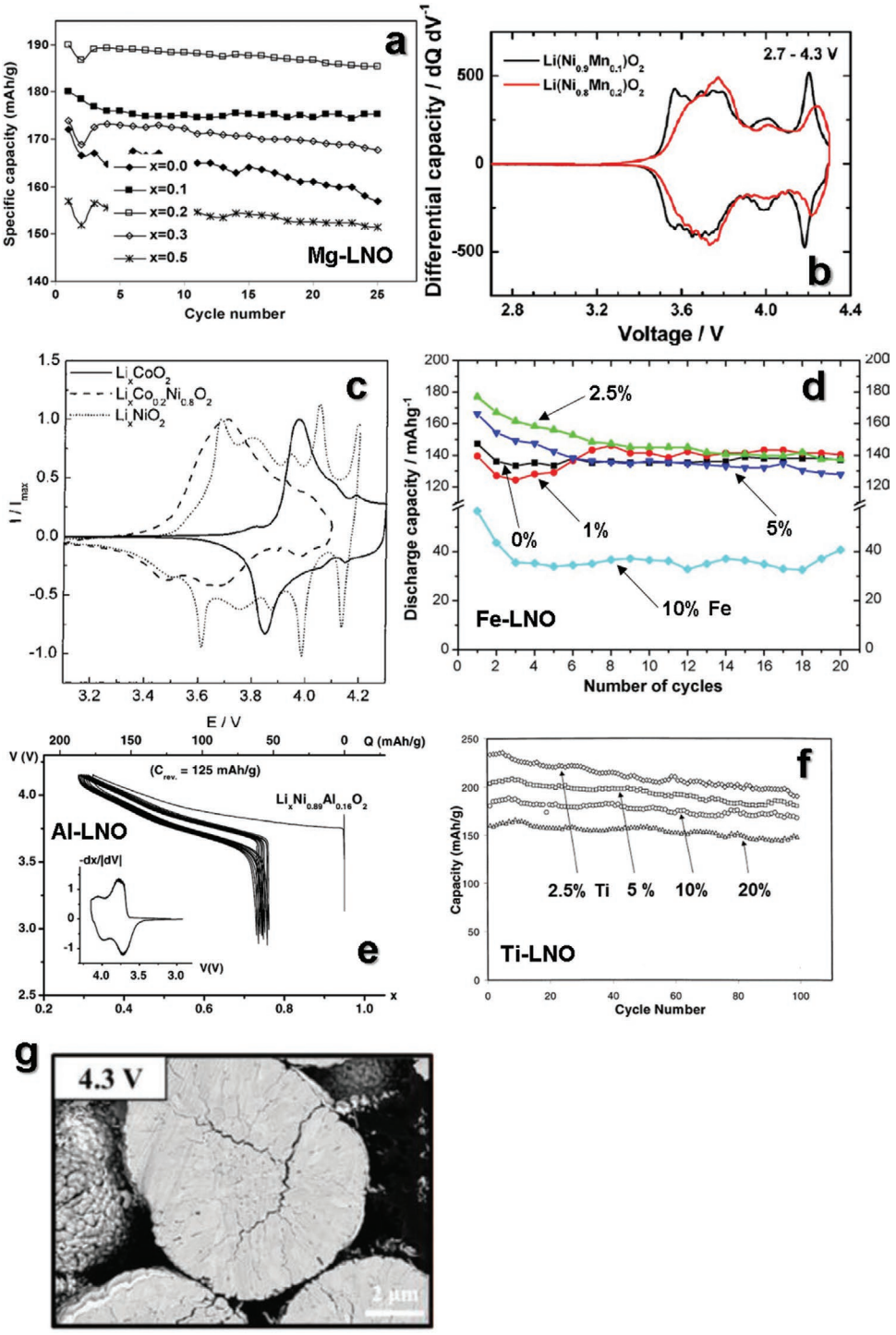

Figure 3. a) Plots of specific capacity versus cycle number of $LiNiO_2$ and $LiNi_{1-x}Mg_xO_2$ ($x = 0.0$, 0.1, 0.2, 0.3, and 0.5). Reproduced with permission.[43] Copyright 2007, Elsevier. b) Differential capacity versus voltage curves for $Li(Ni_{0.9}Mn_{0.1})O_2$ and $Li(Ni_{0.8}Mn_{0.2})O_2$. Reproduced with permission.[32] Copyright 2013, American Chemical Society. c) Steady-state cyclic voltammograms for all of the studied compounds. Scan rate: 10 µV s^{-1}. Each curve was normalized to the maximum current of the main anodic wave. Reproduced with permission.[34,60] Copyright 2001, American Chemical Society. d) Variations in the discharge capacity at a 0.1C-rate with the number of cycles in the voltage range of 2.7–4.2 V for $LiNi_{1-y}Fe_yO_2$ ($0.000 \le y \le 0.100$) calcined in air at 700 °C for 48 h. Reproduced with permission.[52] Copyright 2010, Elsevier. e) Variations in the cell voltage versus lithium amount at the C/20 rate for the first ten galvanostatic charge/discharge cycles of $Li//Li_xNi_{0.89}Al_{0.16}O_2$ cells. The average reversible specific capacity over ten cycles is specified for each cell. The $-dx/|dV| = f(V)$ incremental capacity versus voltage curves are given in inserts. Reproduced with permission.[37] Copyright 2003, Elsevier. f) Electrochemical cyclability of $LiNi_{1-x}Ti_xO_2$ ($0.025 \le x \le 0.2$) samples. Reproduced with permission.[40] Copyright 2001, Elsevier. g) Magnified cross-sectional SEM images of the first charged state of the NM90 cathode at 4.3 V. Reproduced with permission.[55] Copyright 2019, John Wiley and Sons.

reported that partial Co substitution was highly effective in decreasing the cation mixing between Li and the transition metal layers. The multiphase transitions such as "M+H2" and "H2+H3" that occur in $LiNiO_2$, leading to irreversible capacity upon charge–discharge, were suppressed by partial Co substitution. $LiNiO_2$ exhibited irreversible capacity due to multiphase transitions such as "M+H2" and "H2+H3," which were confirmed at voltages exceeding 4.0 V (Figure 3c).[34] The two observed sharp peaks indicated that the phase transition regions corresponding to "M+H2" and "H2+H3" were reduced by increasing the Co content in $LiNiO_2$. This was related to the markedly improved cycling retention with increasing Co content in the $LiNi_{1-x}Co_xO_2$ structure, even at a high rate, compared with that of $LiNiO_2$.[48] These results also agree with those of earlier studies reported by Dahn et al.[7,49] and Delmas et al.[24,50] The electrochemical performance, including the cyclability and high-power capability, was significantly improved by partial Co substitution in $LiNiO_2$.

However, increasing the cobalt content in the compound is not an attractive option for cathode applications in terms of cost-effectiveness. The earth abundance of Fe makes it an attractive substitute.[51] However, the effect of Fe in the layered structure is generally different from that of other transition metals. In the $LiNi_{1-x}Fe_xO_2$ ($0 \le x \le 1$) system, layered structures are only formed in the range of $x < 0.3$. Further increasing the Fe content leads to the formation of a cubic rock salt phase, $LiFeO_2$ (*Fm*-3*m*), because of the Fe ions occupying the Li layers. The Ni-rich $LiNiO_2$ with ≤1% Fe-substitution prepared by a combustion method showed a variation in discharge capacity with similar cycling performance in the voltage rage of 2.7–4.2 V at 0.1C (Figure 3d).[52] Furthermore, Mohan and Kalaignan reported that the $LiFe_{0.15}Ni_{0.85}O_2$ electrode delivered a high reversible capacity of 190 mA h g^{-1} in the voltage range of 3–4.5 V at a rate of 0.5C with 94% capacity retention over 60 cycles.[36] $LiNiO_2$ with >20% Fe-substitution exhibited reduced discharge capacity with poor cyclability because of the formation of the inert rock salt structure, which prevented Li^+ migration in the structure upon charge–discharge. That is, the optimal amount of Fe in the formula should be determined to maximize cell performance.

Al^{3+} is most commonly used in layered cathodes because of its lower cost and atomic weight than those of other transition metals. Therefore, $Li[Ni_{1-x}Al_x]O_2$ has a slightly higher theoretical gravimetric capacity than that of $LiNiO_2$. Ceder and co-workers predicted that the introduction of Al^{3+} in layered $LiMO_2$ cathodes would lead to an increased Li^+ intercalation potential because of the participation of oxygen in electron exchange, which is driven by the fixed Al valence state.[53] Al^{3+} in layered $LiMO_2$ cathodes also prevents cell overcharging. Delmas and co-workers reported that $LiNi_{1-y}Al_yO_2$ suppresses all phase transitions observed for $LiNiO_2$ with good cyclability (Figure 3e).[37] Decreasing the active Ni^{3+} content by direct replacement with electrochemically inactive Al^{3+} in transition metal sites resulted in decreased discharge capacity.[37,54] However, introduction of the optimal amount of Al in $LiNiO_2$ can improve the structural stability, and thus, should be considered as a feasible strategy. The partial substitution of Ti into $LiNiO_2$ leads to structural stabilization due to the stronger Ti^{4+}—O bonds. Cathodes of layered $LiNi^{2+}_{1-x}Ti^{4+}_xO_2$ ($x \le 0.2$) (*R*-3*m*) present suppressed migration of Ni^{2+} into Li sites. Therefore, the layered $LiNi^{2+}_{1-x}Ti^{4+}_xO_2$ ($x \le 0.2$) cathodes delivered high reversible capacities of up to 240 mA h g^{-1} in the range of 2.8–4.3 V, with excellent capacity retention over 100 cycles (Figure 3f).[40] Although the structural stability was further improved when the Ti content in $LiNiO_2$ was increased, the resulting discharge capacity declined as a result of electrochemical inactivation caused by the increased Ni^{2+} ratio in the Li layers. Ni-based cathodes charged over 4.3 V typically show microcracks traversing the entire particle, exposing the interior surface to electrolyte attacks. Meanwhile, the extent of microcracking decreased, despite the small amount of dopant in the $LiNiO_2$, suggesting the damage to the cathode was limited to hairline microcracks emanating from the particle center and was only visible when the cathode was charged to 4.3 V (Figure 3g).[55]

As mentioned above, since the effect of the amount of dopant in $LiNiO_2$ showed improved structural and thermal stability, several researchers have compared the partial substitution of Ni in Ni–Mn-based $LiNi_{0.5}Mn_{0.5}O_2$ cathodes to evaluate the effect of the concentration of each element on the cell performance. Myung et al. studied layered $Li[(Ni_{0.5}Mn_{0.5})_{1-x}Li_x]O_2$ (*R*-3*m*) cathodes to investigate the effect of Li in the transition metal layer.[56] The presence of Li^+ in the transition metal layer effectively improved the structural stability by decreasing Li^+/Ni^{2+} cation mixing and improved the cell performance by enhancing Li^+ diffusion (**Figure 4**a).[56] Yin and co-workers reported that partial Ba-doping in the $Li[Ni_{0.5}Mn_{0.5}]O_2$ structure improved the structural stability and reduced the Li^+/Ni^{2+} cation mixing.[57] Specifically, Ba^{2+} is an attractive dopant or substituent owing to its higher bond dissociation energy of the Ba—O bond (562 kJ mol^{-1}) than that of the Ni—O bond (382.0 kJ mol^{-1}) (Figure 4b).[58] Li and co-workers suggested that Mg^{2+}-doped $Li[Ni_{0.45}Mg_{0.05}Mn_{0.5}]O_2$ displays enhanced cell performance because the inert Mg^{2+} acts as a pillar to stabilize the layered structure.[59] Moreover, Stoyanova et al. reported that Mg^{2+} dopant shows a favorable effect on the stabilization of the layered structure upper cutoff voltage of 4.8 V (Figure 4c).[60] Co^{3+}-doped $LiNi_{0.5}Mn_{0.5-x}Co_xO_2$ exhibited improved rate performance compared with undoped $LiNi_{0.5}Mn_{0.5}O_2$ in the range of 3.0–4.6 V (Figure 4d).[61] Al-substituted $LiNi_{0.5}Mn_{0.5}O_2$ electrodes were prepared via a simple coprecipitation method followed by a combination of coprecipitation and solid-state reaction.[62] Figure 4e shows that the increased capacity retention may be derived from the reduced Li^+/Ni^{2+} cation mixing due to Al doping and the higher bond dissociation energy of the Al—O bond (511 kJ mol^{-1}), which consequently improved the structural stability.[63] Furthermore, Ti-doping caused a slight variation in the *c*-axis of the $Li[Ni_{0.5}Mn_{0.5}]O_2$ structure, which can be attributed to the improved structural stability and electrochemical properties due to the high bonding strength of Ti—O (–889.5 kJ mol^{-1}).[64] With a further increase in the amount of Ti in $Li[Ni_{0.5}Mn_{0.5-x}Ti_x]O_2$, the irreversible capacity and polarization increased, as reported by Delmas and co-workers, and these behaviors were associated with higher Li^+/Ni^{2+} cation mixing (Figure 4f).[31,44] However, $Li[Ni_{0.5}Mn_{0.5-x}Ti_x]O_2$ (x = 0.05–0.1) showed lower polarization with reduced Li^+/Ni^{2+} cation mixing. Therefore, it was confirmed that partial doping with transition metal elements effectively improves the structural stability and electrochemical performance of

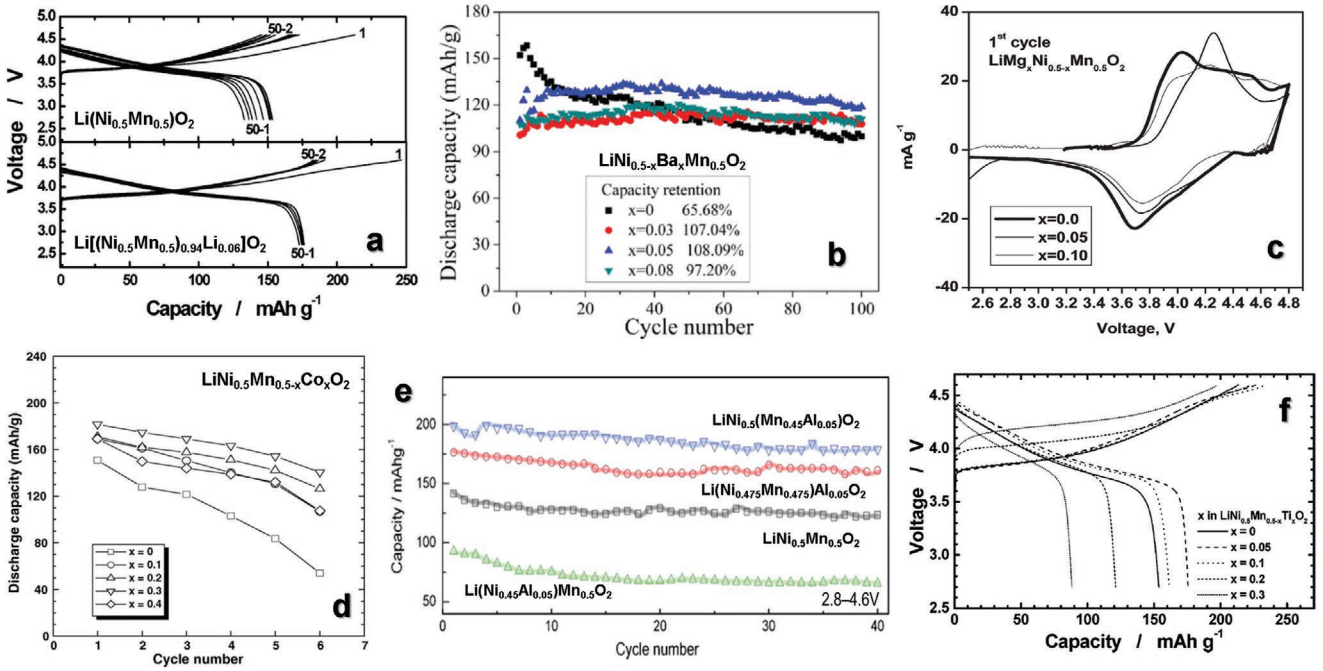

Figure 4. a) Continuous charge and discharge curves of Li/Li[$Ni_{0.5}Mn_{0.5}$]O_2 and Li/Li[$(Ni_{0.5}Mn_{0.5})_{0.94}Li_{0.06}$]$O_2$ cells. The applied current density across the positive electrode was 20 mA g^{-1} at 25 °C. Reproduced with permission.[56] Copyright 2006, American Chemical Society. b) Discharge capacity curves of $LiNi_{0.5-x}Ba_xMn_{0.5}O_2$ ($x = 0$, 0.03, 0.05, 0.08) cathode materials in the range of 2.5–4.8 V at 0.2C at room temperature. Reproduced with permission.[58] Copyright 2018, John Wiley and Sons. c) Potentiostatic curves corresponding to the first charge/discharge cycle of $LiMg_xNi_{0.5-x}Mn_{0.5}O_2$ in lithium cells. Reproduced with permission.[60] Copyright 2006, Royal Society of Chemistry. d) Rate capability of $LiNi_{0.5}Mn_{0.5-x}Co_xO_2$ ($0 \le x \le 0.3$) operated at 3–4.6 V. Reproduced with permission.[61] Copyright 2006, Elsevier. e) Cyclic performance of $LiNi_{0.5}Mn_{0.5}O_2$ and Al substituted compounds operated at a current density of 40 mA g^{-1} in the voltage range of 2.8–4.6 V. Reproduced with permission.[62] Copyright 2008, Elsevier. f) Initial charge and discharge curves of Li/$LiNi_{0.5}Mn_{0.5-x}Ti_xO_2$ ($x = 0$–0.3) cells. A constant current density of 20 mA g^{-1} was applied across the cathode between 2.7 and 4.6 V at 25 °C. Reproduced with permission.[81] Copyright 2005, American Chemical Society.

Li[$Ni_{0.5}Mn_{0.5}$]O_2 cathodes. To compete with NCM and NCA compounds that will be introduced in the next three sections, due to the lack of Co or other electroconducting elements in the transition metal layers, more efforts should be devoted to improve the rate capability and electrode performances at low temperatures.

2.2.2. Improved Thermal Stability

Delmas and co-workers studied the effect of Al doping in $LiNiO_2$ on thermal stability and the related thermal degradation of $Li_{0.3}Ni_{1.02}O_2$ and $Li_{0.3}Ni_{0.89}Al_{0.16}O_2$ that was investigated by high temperature in situ X-ray diffraction increasing temperature (**Figure 5**a).[65] Both samples showed a two-step process; namely, the first-step corresponded to the phase transformation to spinel-type (*Fd*3*m*) phase accompanied by oxygen evolution from the structure around 200 °C and the second-step related to the formation of the rocksalt NiO-like (*Fm*3*m*) phase with more evolution of oxygen from the structure at elevated temperature. Interestingly, the second-step was delayed for $Li_{0.3}Ni_{0.89}Al_{0.16}O_2$, because the stronger bond of Al^{3+}—O suppresses the cation migration that is necessary for the phase transition with increasing temperature.

Co-incorporation into $LiNi_{1-x}Co_xO_2$ electrode ($x = 0$, 0.1, 0.2, and 0.3) demonstrated the similar effect to Al that mitigates and delays the exothermic reaction, thereby substantially reducing heat generation (Figure 5b).[66] The thermal stability of charged $Li(Ni_{1-x}Mn_x)O_2$ ($0.1 \le x \le 0.5$) electrodes were considerably dependent on the Mn content in Figure 5c.[32] Compared to the charged $LiNi_{1-x}Co_xO_2$ electrodes (Figure 5b), the exothermic reaction was significantly suppressed for the Mn-substituted $Li(Ni_{1-x}Mn_x)O_2$ ($0.1 \le x \le 0.5$), showing reduced heat generation at higher temperature (Figure 5c). Effect of Li on the thermal stability is highlighted in Li[$(Ni_{0.5}Mn_{0.5})_{1-x}Li_x$]$O_2$ ($x = 0$ and 0.06) in Figure 5d.[56] The small amount of Li substitution to the transition-metal site resulted in not only reduced heat generation from 1484 to 1147 J g^{-1} but also increased the main exothermic temperature to around 290 °C, compared to the delithiated Li[$Ni_{0.5}Mn_{0.5}$]O_2. Figure 5e shows the DSC results of fully delithiated All $Li_{1-\delta}$[$Ni_{0.5}Mn_{0.5-x}Ti_x$]O_2 ($0 \le x \le 0.3$) electrodes charged to 4.6 V. The thermal stability of the charged cathode material in the electrolyte gradually improved with an increasing amount of Ti content. All $Li_{1-\delta}[Ni_{0.5}Mn_{0.5-x}Ti_x]O_2$ ($0 \le x \le 0.3$) electrodes exhibited simple DSC curves with exothermic temperature higher than 270 °C. The above findings indicate that electro-inactive elements tend to improve structural and thermal stabilities at highly delithiated states, although the effect may negate the characteristic of $LiNiO_2$ that delivers high capacity during initial several cycles. Some combinations such as Li or Ti with low concentration are anticipated to improve both capacity

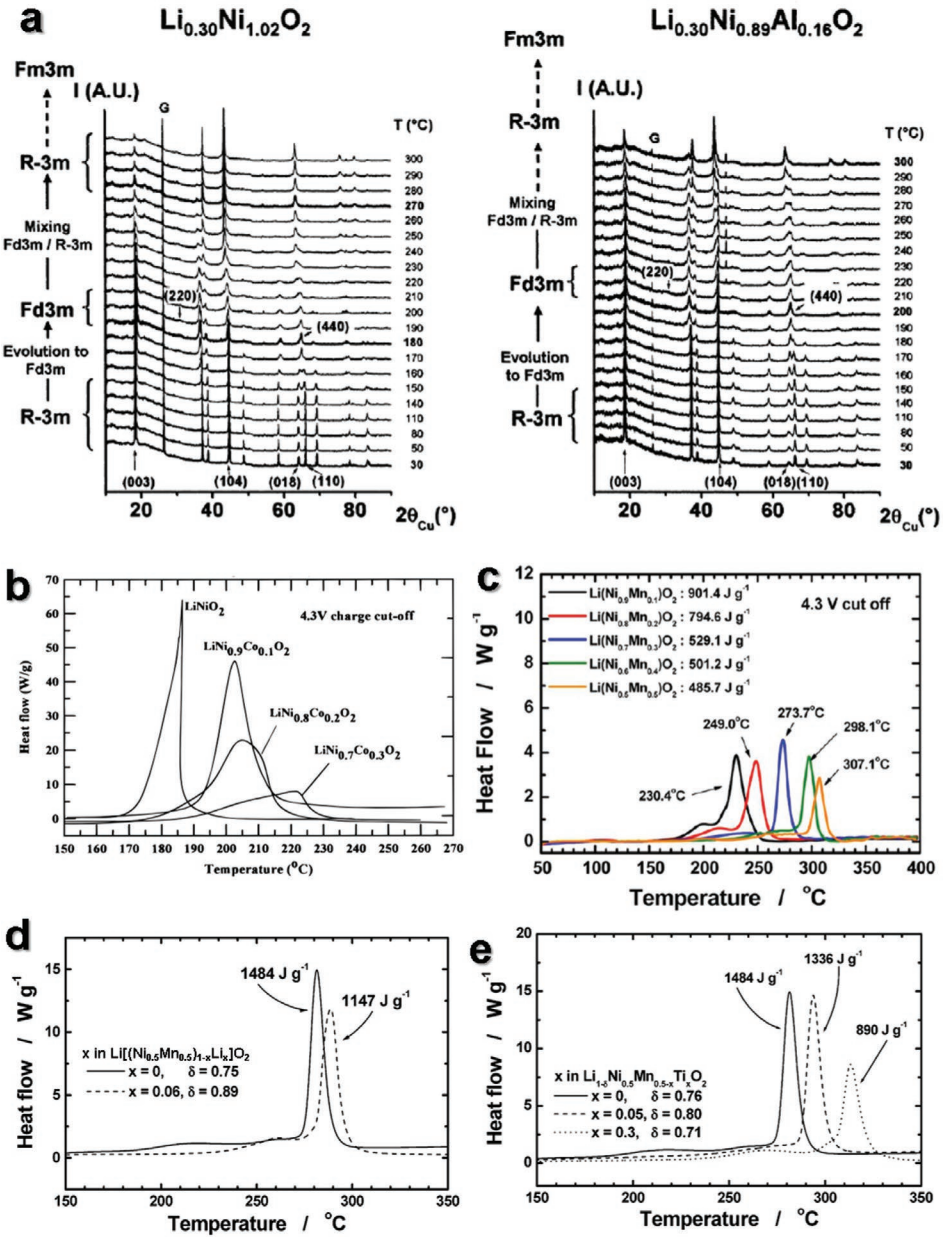

Figure 5. a) In situ X-ray diffraction patterns of $Li_{0.30}Ni_{1.02}O_2$ and $Li_{0.30}Ni_{0.89}Al_{0.16}O_2$ upon increasing temperature (heating rate 15 °C min^{-1}, waiting time before measurement at each temperature step 10 min, data acquisition time 1 h). Reproduced with permission.[65] Copyright 2003, American Chemical Society. b) DSC curves of $LiNi_{1-x}Co_xO_2$ electrodes containing electrolyte for $x = 0$, 0.1, 0.2, and 0.3 after charging them at 4.2 and 4.3 V. Reproduced with permission.[66] Copyright 2000, The Electrochemical Society. c) DSC profiles of the Ni-rich $Li(Ni_{1-x}Mn_x)O_2$ ($x = 0.1$, 0.2, 0.3, 0.4, and 0.5) electrodes at a scan rate 5 °C min^{-1}. The cells were charged to 4.3 V at the rate of 0.2C. Reproduced with permission.[32] Copyright 2013, American Chemical Society. d) DSC traces of the $Li/Li[(Ni_{0.5}Mn_{0.5})_{1-x}Li_x]O_2$ ($x = 0$ and 0.06) cells at 4.6 V. Reproduced with permission.[56] Copyright 2006, American Chemical Society. e) DSC traces of the $Li/LiNi_{0.5}Mn_{0.5-x}Ti_xO_2$ ($x = 0$–0.3) cells at 4.6 V. Reproduced with permission.[81] Copyright 2005, American Chemical Society.

and structural/thermal stability due to their effects on lowering cation mixing or formation of stronger bond between metal and oxygen. These variations in local environments affect not only cycling stability for extended cycles but also thereby delaying the unfavorable exothermic reaction at delithiated states. Therefore, it is concluded that it is a choice of matter to consider the appropriate amount of substituents for advanced cathode materials, performing with high capacity for cycling and thermal stability at highly delithiated state.

3. Existing Present Ternary NCM and NCA

Each transition metal in the ternary Ni–Co–M cathodes plays an important role in achieving excellent cell performance. The structural and electrochemical properties of the formed layered oxide cathode materials depend on the ratio of each transition metal in the composite. To further develop cathode materials with high energy density, several researchers have investigated the effects of increasing the Ni content in the Ni–Co–Mn or Ni–Co–Al system.[67]

3.1. Toward Ni-Rich Cathodes Achieving High Energy Density

Yoon and co-workers verified the changes in the oxidation state depending on the ratio of Ni in $Li[Ni_{0.5+x}Co_{0.2}Mn_{0.3-x}]O_2$ by X-ray absorption near edge structure analysis.[68] The Ni K-edge spectra of $Li[Ni_{0.5}Co_{0.2}Mn_{0.3}]O_2$ were similar to that of Ni^{2+}, and the oxidation state of Ni was the lowest among the evaluated samples. The Ni K-edge spectra shifted to a higher angle (close to that of Ni^{3+}) when the Ni content in $Li[Ni_{0.5+x}Co_{0.2}Mn_{0.3-x}]O_2$ was increased. The Co and Mn K-edge spectra of the $Li[Ni_{0.5+x}Co_{0.2}Mn_{0.3-x}]O_2$ sample were similar to each other, indicating that the average valences of Co and Mn were 3+ and 4+, respectively. Furthermore, the increased average valence of Ni suppressed the migration of Ni^{2+} to the Li layer, leading to suppression of Li^+/Ni^{2+} cation mixing and an increase in the initial capacities. However, the Li^+ intercalation stability in the layered structure depended on the increasing Ni contents. Capacity retention deteriorated because of the increase in the Ni content in ternary NCM and NCA cathodes.[69,70] The ternary Ni-rich NCM and NCA cathodes showed capacity fading mainly associated with the H2–H3 phase transition. To clearly determine the different redox behaviors of the NCM cathodes (NCM333, NCM523, NCM622, NCM701515, and NCM811), the cycling performance and dQ dV^{-1} profiles are shown in **Figure 6**a-1.[69] NCM333 cathode showed reversible redox peaks at ≈3.75 V during cycling. As the ratio of Ni content further increased, a new oxidation peak appeared at ≈3.65 V. Furthermore, the NCM811 cathode showed four distinct peaks with a sharp oxidation peak upon charge, which was caused by the multistep phase transition; hexagonal to monoclinic (H1-M),

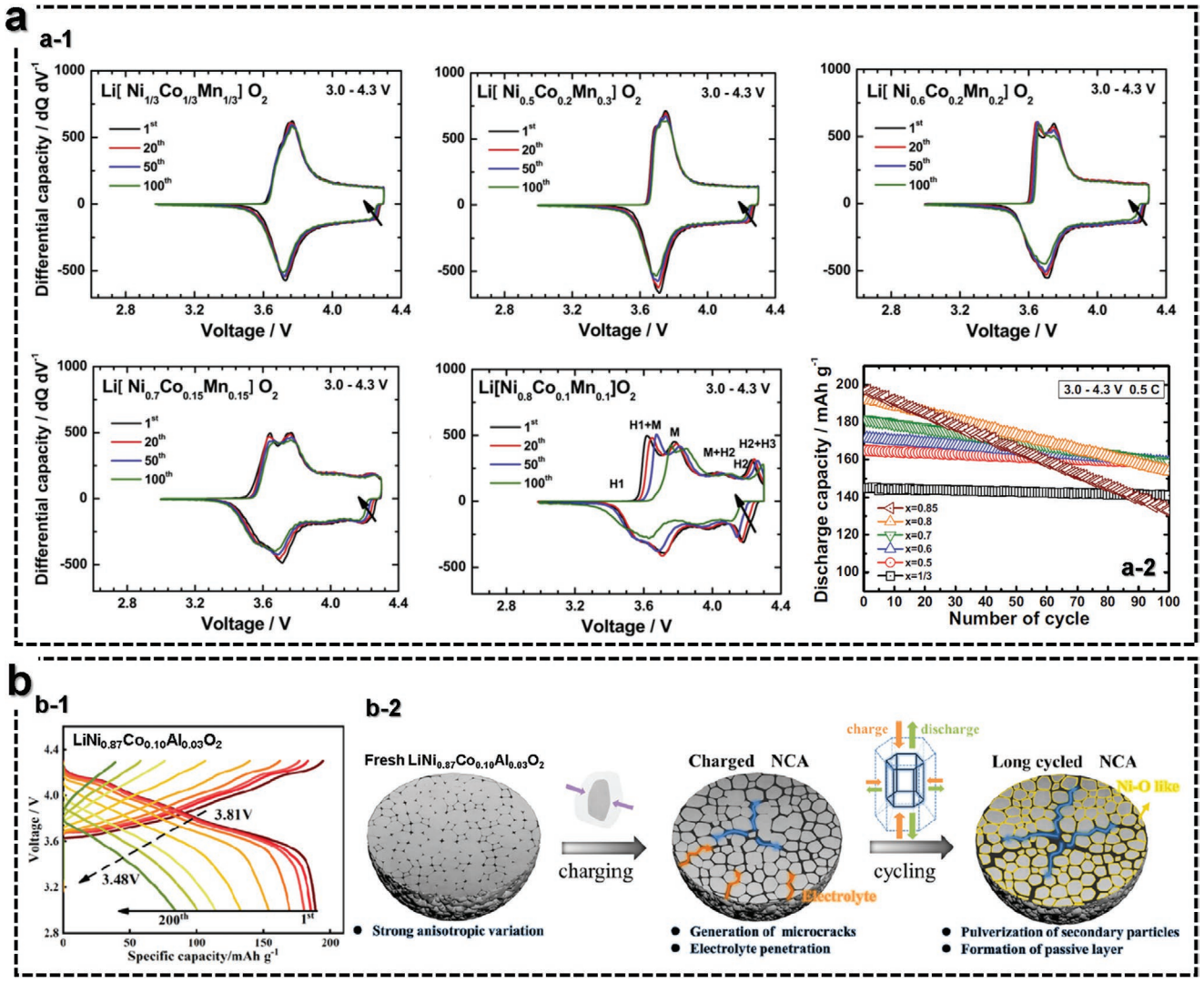

Figure 6. a) Electrochemical properties of NCM cathodes. a-1) Differential capacity versus voltage curves for $x = 1/3$, $x = 0.5$, $x = 0.6$, $x = 0.7$, and $x = 0.8$. The applied current density across the positive electrode was 20 mA g^{-1} (0.1C) at 25 °C in the voltage range of 3.0–4.3 V, a-2) discharge capacity versus cycle number for the $Li/Li[Ni_xCo_yMn_z]O_2$ ($x = 1/3$, 0.5, 0.6, 0.7, 0.8, and 0.85) cells at 25 °C. The applied current density across the positive electrode was 100 mA g^{-1} (0.5C) in the voltage range of 3.0–4.3 V. Reproduced with permission.[69] Copyright 2013, Elsevier b) Charge/discharge profiles; b-1) of 1st, 25th, 50th, 75th, 100th, 125th, 150th, 175th, 200th cycles. Cycle performance for LCNA at a low rate (0.2C). b-2) Schematic description of the degradation of LNCA during a cycle. Reproduced with permission.[71] Copyright 2020, American Chemical Society.

monoclinic to hexagonal (M-H2), and hexagonal to hexagonal (H2–H3). It resulted in the dramatic variation in the *c*-axis, leading to the irreversible capacity during cycles. In addition, the peaks were further polarized and shifted from the original peak position upon cycling. As expected, the cycle retention was decreased with an increasing Ni content (Figure 6a-2).

Similar to the NCM cathode, the NCA cathodes with increasing Ni content suffered from capacity fading, attributed to the H2–H3 phase transition.[71] Figure 6b-1 showed the charge and discharge curves of $Li[Ni_{0.87}Co_{0.10}Al_{0.03}]O_2$ (NCA87) tested in the voltage range of 3.0–4.3 V at 1C current for 200 cycles. The corresponding average operation voltage fell from 3.81 to 3.48 V as cycle progressed. This tendency was ascribed to the morphological degradation of NCA87 particles that experiences unwanted large variations in the *c*-axis during H2–H3 phase transition, leading to generation and propagation of microcracks (Figure 6b-2). Once microcrack was formed to the surface from the core, the electrolyte penetration into the interior of secondary particle accelerates irreversible phase transition and pulverization of secondary particles. In addition, the phase transition with progressively accumulating cation mixing and continuous transition metal dissolution eventually result in decrease in capacity and average operation voltage.

3.2. The Problems Faced by Present Ternary NCM and NCA

The operando XRD results demonstrate that a higher nickel content in the NCM sample (NCM721) led to a monotonous single-phase reaction compared with the multiphase transition that occurred with a lower nickel content in the NCM samples (**Figure 7**a).[72] The (003) peaks gradually shifted toward a lower angle, returned to the original peak position, and shifted to a higher angle, whereas no splitting of the (108), (110), and (113) peaks was observed upon the first charge. A ready and smooth phase transition was possible with increasing Ni content. However, despite the ceaseless effort to overcome the capacity fading of Ni-rich cathode materials, these materials still suffered from unwanted structural degradation at a high cutoff voltage. Stach and co-workers demonstrated a change in the surface structure of the highly delithiated NCA cathode material via combined analysis using high-resolution TEM, selected area electron diffraction (SAED), and electron energy loss spectroscopy techniques (Figure 7b).[73] In the highly delithiated NCA cathodes, the extraction of Li^+ ions from the particle surface led to structural instability, which resulted in a reduction in the transition metal ions and deleterious oxygen loss to achieve charge balance. The surface rock salt layer was also formed as an impurity in correlation with the oxygen loss and reduction in the transition metal ions, with the concomitant development of surface porosity. It is clear that the particles of the Ni-rich cathode materials suffered from structural instability because of Li^+ extraction, highly deleterious oxygen loss, and multiphase transition at the inner and outer sides of the particles. Furthermore, the Ni-rich cathode materials with large primary particles also suffered from the development of severe microcracks from the inner core, which gradually expanded upon extensive cycling. Both NCM811 in the fully charged state at 4.3 V and after cycling, NCA 88 cathodes showed severe microcracks due to the large variation in the *c*-axis, although the microcracks were nonuniform (Figure 7c).[70,74] Transition metals such as Co, Mn, and Al in $LiNiO_2$ cathode help in achieving structural stability through the smooth phase transition; however, the unwanted structural degradation and deleterious oxygen loss at high cutoff voltage have been not suppressed until now.

Thermal stability is one of the most important issues for large-scale energy applications because of the release of oxygen

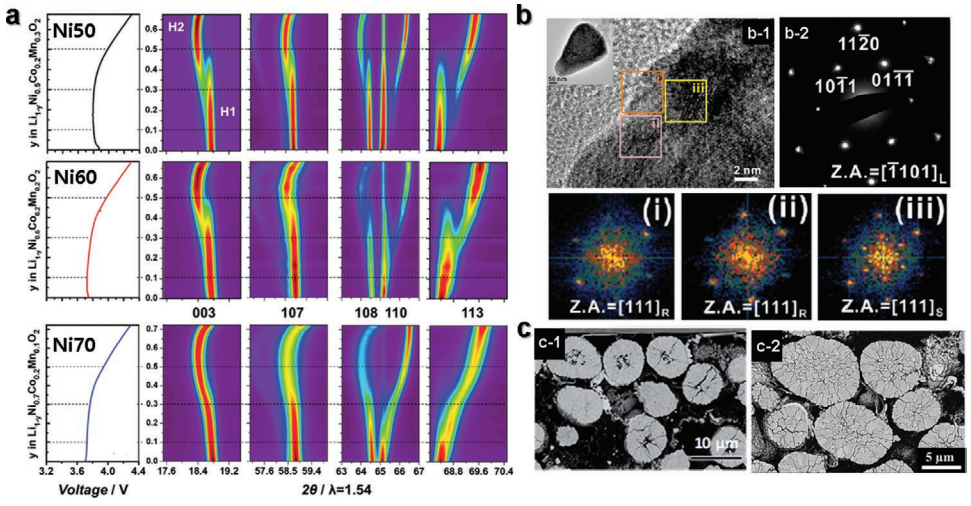

Figure 7. a) In situ XRD profile of $LiNi_{0.5+x}Co_{0.2}Mn_{0.3-x}O_2$ ($x = 0$, 0.1, and 0.2 for 523, 622, and 721, respectively) samples during charge at a rate of C/7. Cell voltage cutoff is 4.3 V. Contour plot of diffraction patterns for (003), (107), (108), (110), and (113) reflections during the first charge of NCM523, NCM622, and NCM721. Corresponding voltage versus Li content curves are plotted to the left of each contour plot. Reproduced with permission.[72] Copyright 2017, John Wiley and Sons. b-1) High-resolution image of an overcharged NCA surface region. The overall particle is shown as an inset. b-2) SADP from whole particle, and i–iii) fast Fourier transformation results of three regions in (b-1). L, S, and R denote the layered $R\bar{3}m$, spinel, and rocksalt structures, respectively. Reproduced with permission.[73] Copyright 2014, American Chemical Society. c) Cross-sectional SEM images of c-1) NCM811 in fully charged states at 4.3 V. Reproduced with permission.[74] Copyright 2019, Royal Society of Chemistry and c-2) NCA88 after cycles. Reproduced with permission.[70] Copyright 2019, American Chemical Society.

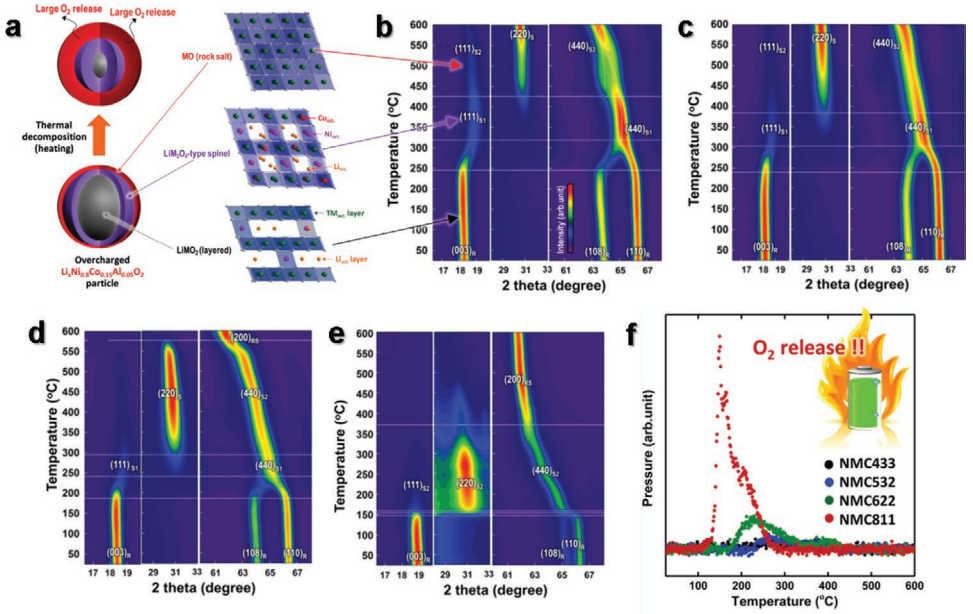

Figure 8. a) Schematic of the mechanism of thermal decomposition of the overcharged $Li_xNi_{0.8}Co_{0.15}Al_{0.05}O_2$ cathode during heating. The left side shows phase propagation from the surface to the core for the overcharged particle. The right side shows the changes in the crystal structure and cation distribution. Reproduced with permission.[76] Copyright 2012, John Wiley and Sons. Contour plots of the TR-XRD patterns at the selected 2θ range for the charged b) NMC433, c) NMC532, d) NMC622, and e) NMC811. f) Mass spectroscopy profiles for the oxygen (O_2, $m/z = 32$) collected simultaneously during measurement of TR-XRD and the corresponding temperature region of the phase transitions for NMC samples. Reproduced with permission.[75] Copyright 2014, American Chemical Society.

from the highly delithiated Ni-rich host structure, which can result in severe thermal runaway. Further release of oxygen possesses a greater risk of battery explosion and becomes safety hazard during battery use. This thermal runaway mechanism is related to the structural instability. Nam and coworkers reported the thermal stability of charged Li[Ni,Mn,Co]O_2 cathode materials upon heating up to 600 °C using a combination study of in situ time-resolved X-ray diffraction and mass spectroscopy (TR-XRD/MS) techniques.[75] All NMC samples (NMC433, NMC532, NMC622, and NMC811) showed a similar route of structural change from the layered structure (*R*-3*m*) to disordered spinel structure (*Fd*3*m*) as the first stage of thermal decomposition (**Figure 8**a). Meanwhile, the onset temperature for the first phase transition from a layered structure to a disordered spinel structure was strongly affected by the ratio of Ni, Mn, and Co in the $LiNiO_2$ structure. For both NMC422 and NMC532, the phase transition to both spinel-1 and spinel-2 occurred at higher temperatures, and spinel-2 remained as the dominating phase till 600 °C (Figure 8b,c). Meanwhile, for both NMC622 and NMC811, the phase transitions to both spinel-1 and spinel-2 occurred and were completed at lower temperatures than those for NMC422 and NMC532; then, the second phase transition from the disordered spinel structure to rocksalt phase was completed at 550 and 365 °C, respectively (Figure 8d–e). In the Ni-rich layered structure, the thermally induced phase transition occurred upon transition from the layered structure (*R*-3*m*) to the disordered spinel structure (*Fd*3*m*) and rocksalt structure (*Fm*-3*m*) with O_2 gas evolution (Figure 8f).[75,76] The inception of detectable oxygen release was observed at ≈180 °C, which is close to the starting temperature of the structural transition from the initial layered structure to the spinel. Further oxygen release in the temperature range of 250–500 °C induced the second phase transition from the disordered spinel structure to the NiO-like rocksalt structure. In other words, the core of the fully delithiated particles showed a layered structure, surface was formed by a rocksalt structure, and near-surface region was formed by the spinel structure at room temperature.[76] Surface modification definitely delayed the phase transition and suppressed oxygen evolution from the delithiated phase. Therefore, the resulting exothermic heat could be greatly reduced, and the resulting temperature was elevated.[77]

3.3. Strategies to Enhance Electrode Performances of Ternary NCM and NCA

The surface stability of Ni-rich layered oxides on the cell performance should be considered. The residual lithium oxide on the surface of primary particles quickly reacts with moisture, O_2, and CO_2 in air (**Figure 9**a).[78] Furthermore, the undesired layers (comprising LiOH, Li_2CO_3, and LiF) gradually formed by repeated side reactions induce degradation in the active material upon decomposition of $LiPF_6$ salts, which hinders Li^+ diffusion and induces gas evolution that may cause serious safety concerns. Surface modification by coating provides solutions for effectively resolving these problems.

3.3.1. Thin and Rough Surface Coating

Conventional coating processes lead to a limited improvement in the cell performance due to the nonuniformity of

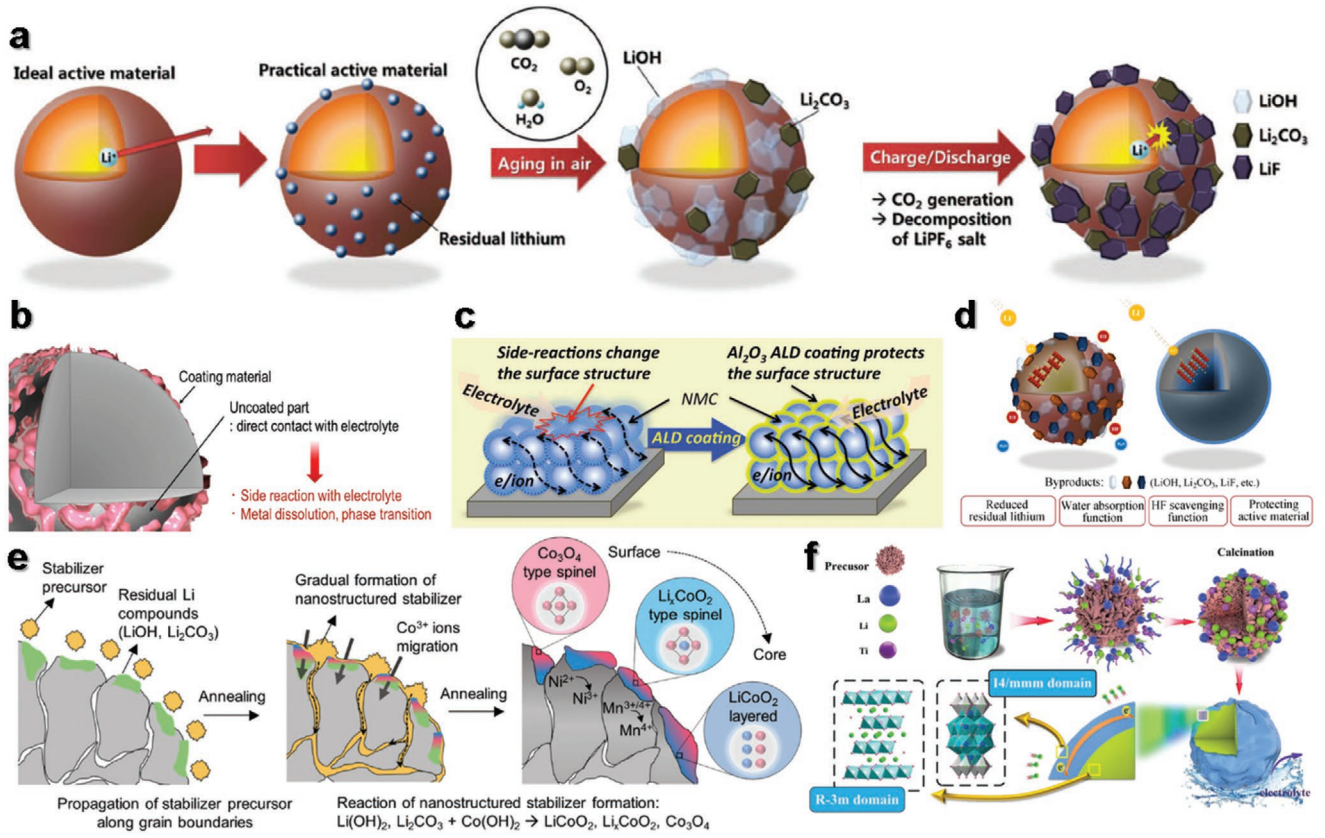

Figure 9. a) Surface change of $Li[Ni_{0.7}Mn_{0.3}]O_2$ materials after exposure to air and effect of the residual lithium on the surface of $Li[Ni_{0.7}Mn_{0.3}]O_2$. Reproduced with permission.[78] Copyright 2014, The Electrochemical Society. b) Schematic diagrams of coated surface morphologies prepared by a general sol–gel method, resulting in an uncoated region and island-like deposition of the coating material. Reproduced with permission.[79] Copyright 2014, John Wiley and Sons. c) Schematic representations of the protective mechanisms of the ALD Al_2O_3-coated $LiNi_{0.4}Co_{0.2}Mn_{0.4}O_2$ electrode. Reproduced with permission.[80] Copyright 2015, American Chemical Society. d) Schematic illustration of byproducts on the surface of bare and lithium phosphate-coated $Li[Ni_{0.6}Co_{0.2}Mn_{0.2}]O_2$ (1 wt%) after 150 cycles. Reproduced with permission.[82] Copyright 2014, Springer. Preparation and characterization of NS-NCM. e) Schematic diagram of the synthesis process of NS-NCM, showing that the decomposition of the cobalt hydroxide compounds creates a nanostructured stabilizer with an epitaxial structure at the cathode and stabilizes the surface TM oxidation states. Reproduced with permission.[83] Copyright 2018, Royal Society of Chemistry. f) Diagram of the proposed synthesis process for dual-modified $LiNi_{0.8}Co_{0.1}Mn_{0.1}O_2$ composite. Reproduced with permission.[85] Copyright 2019, John Wiley and Sons.

the coating layer on the surface (Figure 9b).[79] The uncoated surface is directly exposed to the hydrofluoric acid (HF)-containing electrolyte and shows capacity fading due to the degradation of active materials by the HF attack during cycling. Importantly, it is recognized that the thickness, uniformity, and conductivity of the coating layer are the most important considerations for surface modification. Therefore, an ultrathin film coating and rough surface coating have been developed to improve the structural and electrochemical properties, as summarized in **Tables 2** and **3**. Atomic layer deposition (ALD) is based on sequential self-limiting surface reactions and is normally used to fabricate ultrathin film coatings. Toney and co-workers reported that an ultrathin Al_2O_3-coated $Li[Ni_{0.4}Mn_{0.4}Co_{0.2}]O_2$ sample mitigated the unwanted side reaction between the active material and electrolyte without restricting Li de/intercalation (Figure 9c).[80] Myung et al. demonstrated that the Al_2O_3 coating layer delayed the structural degradation and surface reactions due to HF attacks.[81] The protection of the surface by the Al_2O_3 coating enabled high-voltage cycling stability without severe capacity loss, even at a 5C-rate. They also reported the formation of Li_3PO_4-coated $Li[Ni_{0.6}Co_{0.2}Mn_{0.2}]O_2$ through a rough coating process.[82] H_3PO_4 is stable as a liquid state, so that it is diluted via mixing with water or ethanol. A simple reaction of the mixture solution and active materials and consecutive heating induces the formation of Li_3PO_4 coating layers via reaction with surface lithium residues such as LiOH and Li_2CO_3 on Ni-rich $Li[Ni_{0.6}Co_{0.2}Mn_{0.2}]O_2$: $3LiOH + H_3PO_4 \rightarrow Li_3PO_4 + 3H_2O$ and $3Li_2CO_3 + 2H_3PO_4 \rightarrow 2Li_3PO_4 + 3CO_2 + 3H_2O$ (Figure 9d). This was effective in decreasing the concentration of residual compounds like LiOH and Li_2CO_3 on the surface of $Li[Ni_{0.6}Co_{0.2}Mn_{0.2}]O_2$. The resulting Li_3PO_4-coated $Li[Ni_{0.6}Co_{0.2}Mn_{0.2}]O_2$ exhibited improved electrochemical performance and structural integrity. The presence of the Li_3PO_4 coating layer protected the active material from HF attacks and water in the electrolyte during extensive cycling. These multifunctional Li_3PO_4 coating layers provided an active material, which positively affected the structural and electrochemical properties. In particular, the highly conducting ionic Li_3PO_4 coating

Table 2. Summary of the coating type including ultrathin film coating.

Coating type	Method	Advantage/ disadvantage	Coating media	Cathode material	Voltage [V]	Initial capacity [mAh g^{-1}]	Best capacity retention	Best rate performance	Ref.
Ultrathin film coating	Atomic layer deposition (ALD)	Uniform, continuous, nanoscale, tunable thickness, precise control/limited sources, impeded conductivity	Al_2O_3–Ga_2O_3	NCM523	3.0–4.3 V	150	90% at 1 C	52% at 10 C	[117]
			ZnO	NCM523	2.5–4.5 V	267.3	87% at 2 C	56% at 5 C	[118]
			Al_2O_3	NCM811	2.7–4.6 V	212.8	84% at 0.1 C	–	[119]
			Al_2O_3	NCM622	2.8–4.2 V	166	84% at 1 C	–	[120]
			Al_2O_3	NCM523	3.0–4.3 V	165	90% at 1 C	30% at 10 C	[121]
			ZrO_2	NCM523	3.0–4.3 V	170	76% at 1 C	64% at 10 C	
			MgO	NCM523	3.0–4.3 V	160	82% at 1 C	64% at 10 C	
			TIO_2	NCM622	2.5–4.3 V	187	85% at 1 C	48% at 10 C	[122]
			Al_2O_3	NCM333	3.0–4.5 V	180	94% at 1 C	25% at 16 C	[86]
			TiO_2	$LiNi_{0.8}Co_{0.15}Al_{0.05}O_2$	2.8–4.5 V	210	90% at 1 C	73% at 5 C	[123]
	Chemical vapor deposition (CVD)		Anthracene	NCM333	2.0–4.3 V	153	96% at 0.2 C	71% at 2 C	[124]

induced facile Li^+ diffusion, resulting in enhanced high-power capability with cyclability. As surface engineering advanced, Cho and co-workers modified $Li[Ni_{0.8}Co_{0.1}Mn_{0.1}]O_2$ by nanoscale epitaxy control via a simple dry powder mixing method, which effectively strengthened the surface morphology (Figure 9e).[83] In the initial step, $Co(OH)_2$ as the stabilizer precursor could be propagated into the grain boundary and reacted with the residual lithium compounds, $Li(OH)_2$ and Li_2CO_3, on the surface during the annealing process,[84] resulting in an epitaxially grown surface nanostructure with a concentration gradient. Lu and co-workers designed a Ti-doped and La_4NiLiO_8-coated $Li[Ni_{0.8}Co_{0.1}Mn_{0.1}]O_2$ composite by simple and convenient dual modification, which is another advanced surface engineering technique, as shown in Figure 9f.[85] Using density-functional theory (DFT) calculations, they proposed that diffusion of Ti ions into the bulk structure and accumulation of La ions, which could react with Ni ions, occurred on the surface. Interestingly, the dual-modified compounds exhibited remarkably improved electrochemical performance even under considerably severe battery conditions. This was attributed to the synergetic effect of the La_4NiLiO_8 conductive coating layer[85] and high bonding strength of Ti—O (–889.5 kJ mol^{-1}).[64] Earlier, the modification process was thought to include the simple application of nanolayers on the surface of active materials to prevent deterioration of active materials. However, later, it developed so that the nanolayers could scavenge HF from electrolyte to minimize the degradation of active materials from HF attack. Recent modifications are progressing to minimize the surface residues such as LiOH and Li_2CO_3 and to functionalize the coating media depending on their inherent properties, such as conductivity, rigidity, and affinity to HF and H_2O in electrolytes. The latter one is particularly suitable for Ni-rich cathode materials to enhance durability of the active materials with high capacity. However, this method is suitable for Ni-based cathode materials with Ni contents of ≤80%, and it is difficult to apply the method to Ni-rich cathode materials (with over Ni 90%) due to the instability of Ni. Therefore, advanced surface modifications that can suppress the atmospheric sensitivity of Ni, its side reactions with lithium, and various side effects should be developed for Ni-rich cathode materials.

3.3.2. Stabilization of Surface and Interfacial Structure

Surface deterioration triggered by HF attacks causes structural degradation, electrolyte decomposition, and formation of rock salt-like NiO_2 phases at high cutoff voltages. Therefore, surface modification by coating is necessary to improve surface stabilities. Highly delithiated bare NCM suffers from the development of severe microcracks from the inner core, which gradually expand upon extensive cycling (**Figure 10**a). In contrast, the particles of fully delithiated ALD-coated NMC333 showed no formation of microcracks even after 100 cycles (Figure 10b). In Figure 10c, the SAED patterns show that a biphasic structure was irreversibly formed between the layer structure (*R*-3*m*) and cubic spinel structure (*Fd*3*m*) for a bare NMC electrode. In contrast, the Al_2O_3 coating layer on the surface of ALD-coated NMC333 preserved the original layered structure during extensive cycling, as shown in Figure 10d.[86] Rough-type coating also had a positive effect on stabilizing the surface chemistry. Some byproducts were formed on the surfaces of the bare NCM622 electrodes, which is attributed to the decomposition of the electrolyte. The particles were seriously damaged because of HF attack during cycling (Figure 10e,f). Li_3PO_4-coated NCM622 sustained its original structure with a uniform coating layer, resulting in high reversible capacity upon cycling because of the protective effect of the coating layer against HF and water in the electrolyte upon extensive cycling, as shown in Figure 10g,h.[82] Cho and co-workers suggested that the Ni ions extracted from the cathode were the main contributors to the deterioration of

Table 3. Summary of the coating type including rough coating.

Coating type	Method	Advantage/ disadvantage	Coating media	Cathode material	Voltage [V]	Initial capacity [mAh g^{-1}]	Best capacity retention	Best rate performance	Ref.
Rough surface coating	Solid state	Simple preparation, ease of scale-up/ not continuous, not uniform	LiF	NCM333	2.5–4.5 V	182	78% at 10 C	68% at 10 C	[125]
	Solid state		Li_2MoO_4	NCM523	3.0–4.4 V	178	83% at 0.2 C	–	[126]
	Solid state		Li_2MoO_4	NCM523	3.0–4.5 V	186	84% at 0.2 C	–	
	Solid state		Li_3PO_4	$LiNi_{0.815}Co_{0.15}Al_{0.035}O_2$	2.75–4.5 V	195	70% at 0.5 C	66% at 10 C	[127]
	Solid state		Li_2TiO_3	NCM811	2.8–4.3 V	163	98% at 1 C	–	[128]
	Solid state		$C_6H_9O_6La\cdot_xH_2O$, $C_{16}H_{36}O_4Ti$ (Dual)	NCM811	2.7–4.3 V	200	90% at 1 C	80% at 10 C	[85]
	Co-precipitation		TiO_2	NCM622	3.0–4.5 V	193.9	89% at 1 C	74% at 5 C	[129]
	Co-precipitation		MOF-derived alumina (MDA)	NCM622	3.0–4.5 V	214	92% at 1 C	70% at 10 C	[130]
	Co-precipitation		$Li_2Si_2O_5$	NCM622	2.75–4.5 V	210	67% at 5 C	57% at 10 C	[131]
	Co-precipitation		Li_xTiO_2–silica	NCM622	2.75–4.3 V	175	91% at 0.5 C	80% at 5 C	[132]
	Co-precipitation		AlF_3	NCM523	2.8–4.5 V	180	98% at 4 C	88% at 6 C	[133]
	Co-precipitation		Li_3PO_4–PPy	NCM811	2.8–4.5 V	206	86% at 1 C	80% at 10 C	[134]
	Co-precipitation		Al_2O_3–$AlPO_4$	NCM523	3.0–4.5 V	180	94% at 0.2 C	75% at 2 C	[135]
	Co-precipitation		Cobalt hydroxide	NCM811	3.0–4.3 V	200	55% at 0.5 C charge/ 1C discharge	–	[83]
	Hydrothermal		$LiAlO_2$-inlaid	NCM523	2.7–4.6 V	221	91% at 1 C	71% at 5 C	[136]
	Hydrothermal		Al_2O_3	NCM622	2.7–4.5 V	196	84% at 0.2 C	65% at 3 C	[137]
	Hydrothermal		$LiAlO_2$	NCM622	2.7–4.5 V	206	87% at 0.2 C	68% at 3 C	
	Solvothermal		H_3PO_4	NCM622	3.0–4.3 V	170	94% at 0.1 C	88% at 10 C	[82]
	Solvothermal		Al_2O_3	$Li[Li_{0.05}Ni_{0.4}Co_{0.15}Mn_{0.4}]O_2$	3.3–4.3 V	155	96% at 1 C	76% at 5 C	[81]
	Sol–gel		Li_2O–ZrO_2	$LiNi_{0.8}Co_{0.15}Al_{0.05}O_2$	2.5–4.0 V	100 mhA	80% at 0.05 mA cm^{-2}	60% at 1 mA cm^{-2}	[138]
	Sol–gel		Li_3PO_4	NCM811	2.8–4.5 V	193	85% at 1 C	71% at 10 C	[139]
	Sol–gel		Li_3PO_4	NCM622	2.8–4.7 V	192	79% at 1 C	47% at 10 C	[140]
	Sol–gel		WO_3	NCM811	2.5–4.3 V	192	80% at 0.5 C	40% at 5 C	[141]

the robustness of the solid electrolyte interphase (SEI) on the anode, leading to a decrease in the Coulombic efficiency (CE) in the full-cell system. Figure 10i shows the structural and morphological degradation of the SEI layer on the anode by the reaction between the extracted Ni ions from the cathode and anode during extensive cycling. Surface modification of the cathode via formation of a nanostructured stabilizer with an epitaxial structure improved the morphological robustness. The uniform and thin SEI layer on the anode was maintained by suppressing the catalytic reaction of the solvent, eventually suppressing the growth of the dendritic Li.[83] Simultaneous dual modifications provided the cathode with inner/outer stability through the synergetic effect of the La_4NiLiO_8 conductive coating layer with the good strength of Ti—O (–889.5 kJ mol^{-1}).[64] As shown in Figure 10j,[85] there was no structural damage to the layer structure (*R*-3*m*) or surface exfoliation even after 200 cycles. In particular, the formation of cubic spinel $LiNi_2O_4$ and rocksalt NiO, which is critical for capacity degradation, was suppressed in the surface region, while the La_4NiLiO_8 coating layer could still protect the surface from electrolyte attacks and side reactions. Each coating type is summarized in Tables 2 and 3. The ALD coating method can fabricate an ideal coating layer by depositing an ultrathin film on the surface. However, considering commercialization and cost-effectiveness for the industry, the coprecipitation coating method is preferable owing to its ease of scale-up for the industry and low cost of operation. In the future, advanced surface modification engineering such as nanoscale epitaxy control and dual modification should be developed to ease the scale-up and provide uniform and thin coating layers.

4. Direction of Co-Less Ni-Rich High Capacity Cathodes for Future

4.1. Co-Less Ni-Rich Cathodes for Future

As shown in **Figure 11**a, the (003) peaks gradually shifted toward a lower angle, returned to the original peak position,

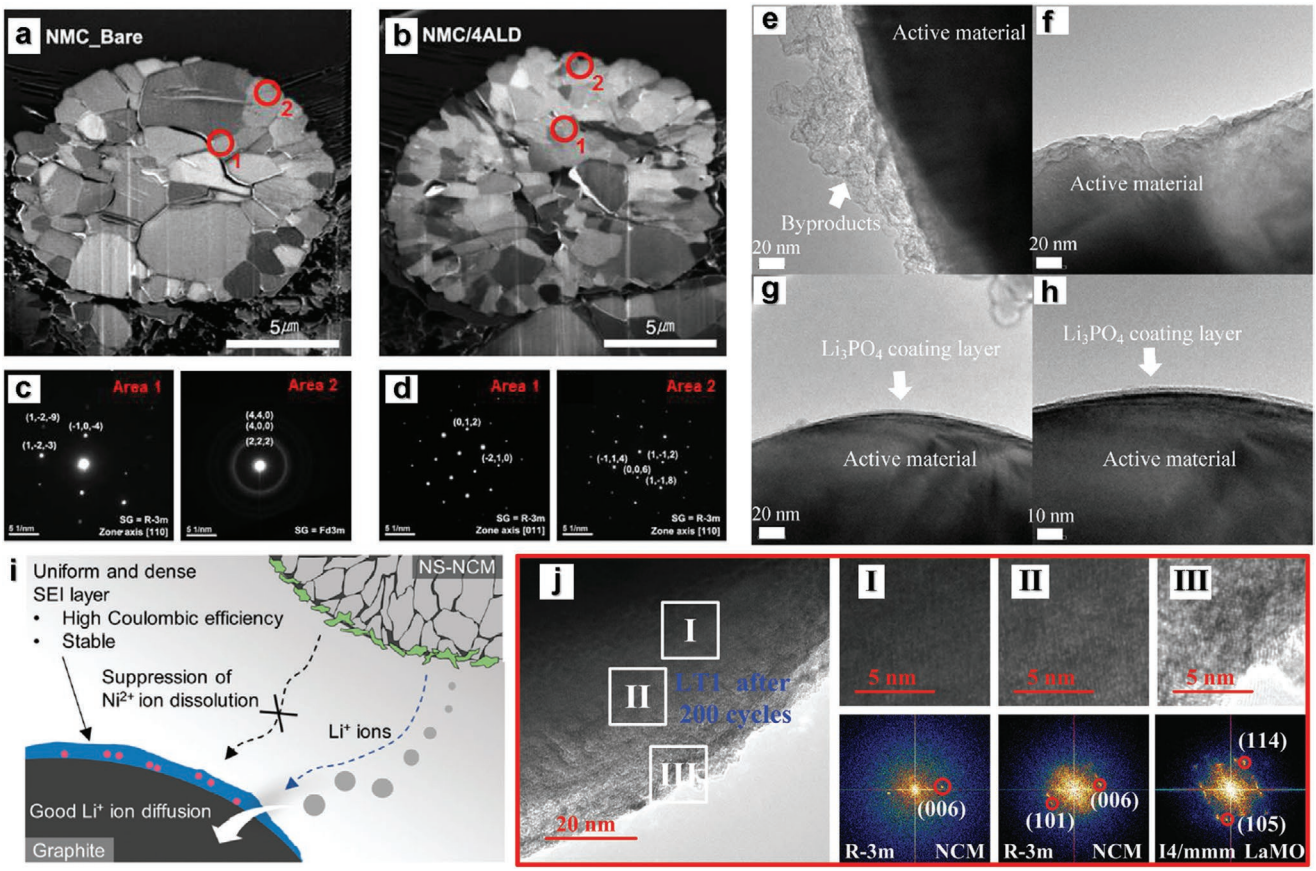

Figure 10. FIB cross-sectional images of fully charged (delithiated) a) NMC bare and b) NMC/4ALD after 100 cycles at 1C-rate between 3.0 and 4.5 V. TEM SAED patterns from the inner 1) and outer areas 2) of each particle show phase transition in NMC bare electrode c), whereas NMC/4ALD presents the same crystal structure from the inner to outer areas d). Reproduced with permission.[86] Copyright 2014, Elsevier. TEM bright-field images of extensively cycled bare and lithium phosphate-coated $Li[Ni_{0.6}Co_{0.2}Mn_{0.2}]O_2$ (1 wt%) electrode at room temperature. Bare electrode: e) lower magnification and f) higher magnification. Lithium phosphate-coated electrode: g) lower magnification and h) higher magnification. Microstructure of the graphite anode after the cycling test. Reproduced with permission.[82] Copyright 2014, Springer. i) Schematic diagram showing the effect of the suppressed nickel-ion dissolution on the morphology of the anode SEI layer. Reproduced with permission.[83] Copyright 2018, Royal Society of Chemistry. j) HRTEM and corresponding FFT images of LT1 after 200 cycles at 1C-rate between 2.7 and 4.3 V. Reproduced with permission.[85] Copyright 2019, John Wiley and Sons.

and then moved to a higher angle, whereas no splitting of the (104) peak was observed in the first charge. Interestingly, $Li[Ni_{0.95}Mg_{0.05}]O_2$ underwent a continual and monotonous single-phase reaction upon charge–discharge. Despite the small amount of transition metal dopants in $LiNiO_2$, $Li[Ni_{0.95}Mn_{0.05}]O_2$ (Figure 11b), $Li[Ni_{0.95}Al_{0.05}]O_2$ (Figure 11c), and $Li[Ni_{0.98}W_{0.02}]O_2$ (Figure 11d) showed better structural stability than $LiNiO_2$ (Figure 2e).[42,87] This was caused by the suppression of the multiphase transition from H2 to H3, which was verified in the high-voltage range, along with a decrease in the Li^+/Ni^{2+} cation mixing. Furthermore, two (003) peaks were observed in the profile of $Li[Ni_{0.95}Co_{0.05}]O_2$, and the (104) peak was split in the highly delithiated state, similar to the case of $LiNiO_2$ (Figure 11e). This means that a suitable amount of Co is required to achieve enhanced structural stability, as shown in the dQ dV^{-1} profiles (Figure 11f). This indicates that unlike Mg, Mn, Al, and W, Co does not effectively suppress the phase transitions upon charge–discharge. Therefore, more attention should be paid to increase capacity with rate capability instead of the Co content. Notably, the W-rich surface phase reflected the thermal stability for fully delithiated Ni-rich Li_xNiO_2 despite the small amount of W. The DSC results for the delithiated W-doped Li_xNiO_2 cathodes (Figure 11g) showed that the doping of $LiNiO_2$ with W effectively reduced the thermal activity by shifting the onset temperature of the oxygen evolution toward a higher temperature region and reducing the heat released by the exothermic reaction.[42]

4.2. Strategies to Enhance Electrode Performances of Co-Less Ni-Rich Cathodes

4.2.1. Co-Less Ni-Rich NCM, NCA, NCW, and NMA Cathodes

The replacement or combination of two elements in $LiNiO_2$ could improve the cell performance more effectively owing to the synergistic effects of each element. Among the known cathode candidate materials, ternary $Li[Ni_{1-x-y}Co_xMn_y]O_2$ (NCM, Ni ≥ 90 %) displays the best overall cell performance because Co substitution reduces cation mixing between Li^+ and Ni^{2+}, whereas Mn^{4+} substitution improves the structural stability of the host. To satisfy the increasing requirement for

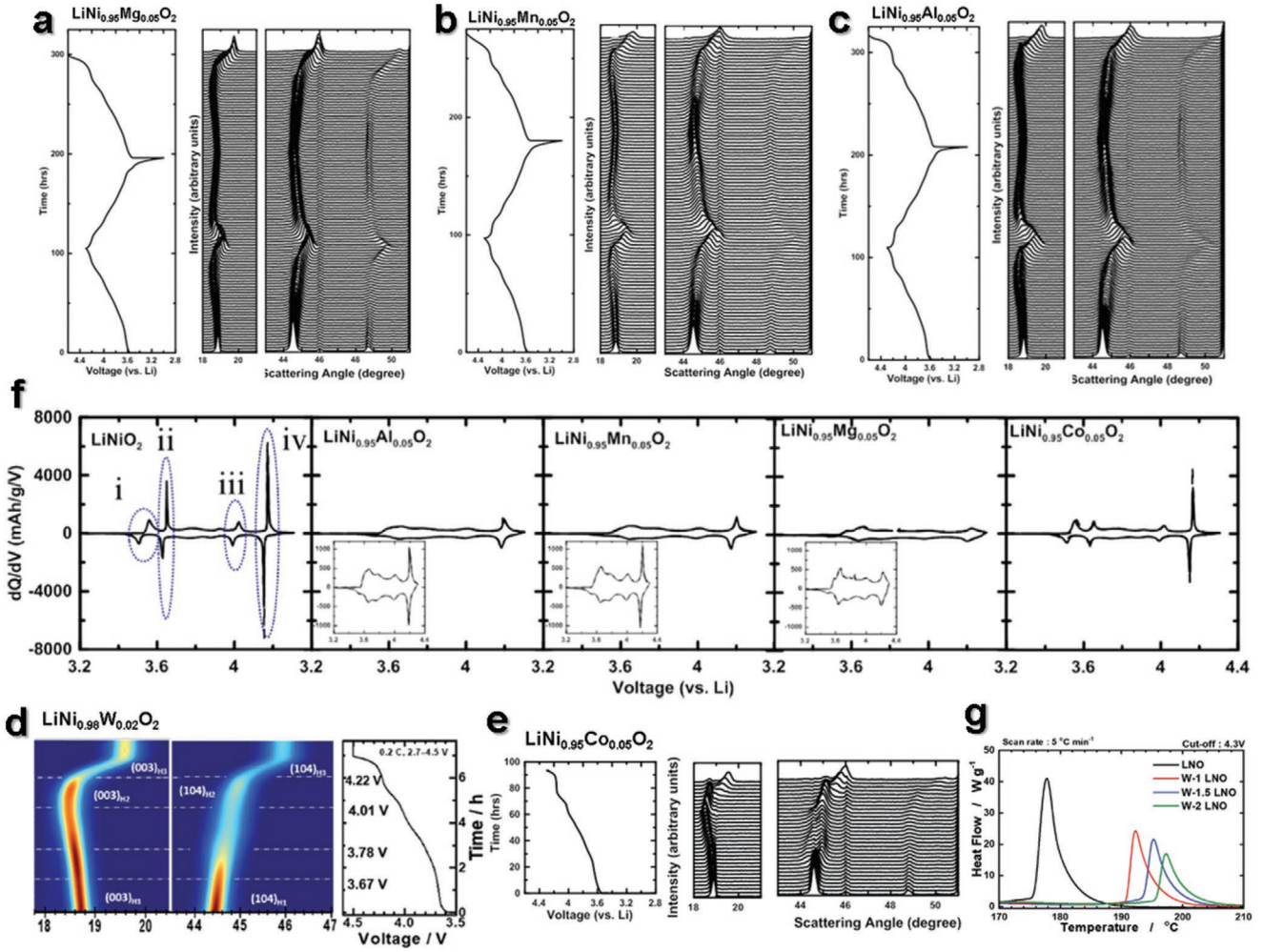

Figure 11. a) Differential capacity as a function of cell voltage ($dQ\ dV^{-1}$ vs V) of the second charge and discharge of $LiNiO_2$, $LiNi_{0.95}Al_{0.05}O_2$, $LiNi_{0.95}Mn_{0.05}O_2$, $LiNi_{0.95}Mg_{0.05}O_2$, and $LiNi_{0.95}Co_{0.05}O_2$. Reproduced with permission.[87] Copyright 2019, The Electrochemical Society. In situ XRD patterns and cell cycling profiles of b) $LiNi_{0.95}Mg_{0.05}O_2$, c) $LiNi_{0.95}Mn_{0.05}O_2$, d) $LiNi_{0.95}Al_{0.05}O_2$, and e) $LiNi_{0.98}W_{0.02}O_2$. Reproduced with permission.[42] Copyright 2019, Royal Society of Chemistry. f) $LiNi_{0.95}Co_{0.05}O_2$. Reproduced with permission.[87] Copyright 2019, The Electrochemical Society. g) DSC profiles of LNO, W-1 LNO, W-1.5 LNO, and W-2 LNO in the delithiated state at 4.3 V. Reproduced with permission.[42] Copyright 2019, Royal Society of Chemistry.

high energy density, the composition range of the Ni-rich layered NCM was extended to the end candidate by synthesizing $Li[Ni_{0.90}Co_{0.05}Mn_{0.05}]O_2$ (NCM90), $Li[Ni_{0.95}Co_{0.025}Mn_{0.025}]O_2$ (NCM95), and $Li[Ni_{0.98}Co_{0.01}Mn_{0.01}]O_2$ (NCM98), all of which delivered a reversible capacity of over 220 mAh g^{-1} when charged to 4.3 V. Sun and Manthiram synthesized NCM90 with a high reversible capacity (227 mAh g^{-1}, 0.1C) and good rate performance at 2.7–4.3 V versus Li^+/Li^0, which meets the 350 Wh kg^{-1} energy density at the cell level.[88] Nonetheless, NCM90 suffers from obvious capacity fading, similar to $LiNiO_2$, caused by the large volume change and subsequent crack propagation in the bulk and formation of the rocksalt NiO phase in the surface/subsurface of the particles. Sun and co-workers increased the Ni content in NCM cathodes, where NCM95, NCM90, and $LiNiO_2$ were compared to evaluate the electrochemical performance and structural evolution.[89] There was no obvious separation of the (006)/(102) and (108)/(110) peaks for $LiNiO_2$, whereas the peak split became clearer for NCM95 to NCM90 due to the formation of a well-ordered structure by decreasing the Ni content in NCM. The as-prepared NCM series cathode materials exhibited spherical morphologies with an average diameter of 10 µm synthesized through coprecipitation (**Figure 12**a).[89] All NCM cathodes delivered a high discharge capacity of over ≈220 mAh g^{-1} at a constant current density of 20 mA g^{-1} (0.1C) at 30 °C, with a high CE over 93%. These cathodes utilize 95% of Li^+ ions for electrochemical reactions and delivered a high discharge capacity of over ≈200 mAh g^{-1}, whereas the cyclability of the NCM90 cathode could be improved to ≈78% from ≈70% after 100 cycles (Figure 12b).[89] The enhanced cell performance was attributed to the positive effect of the decreased Li^+/Ni^{2+} cation mixing and the effect of the increased Co and Mn content in $LiNiO_2$ on suppressing the phase transition, curtailing the evolution of the H2 phase to the H3 phase at a high voltage.

Figure 12c shows the DSC results of the fully delithiated $Li_x[Ni_{0.90}Co_{0.05}Mn_{0.05}]O_2$, $Li_x[Ni_{0.95}Co_{0.025}Mn_{0.025}]O_2$, and

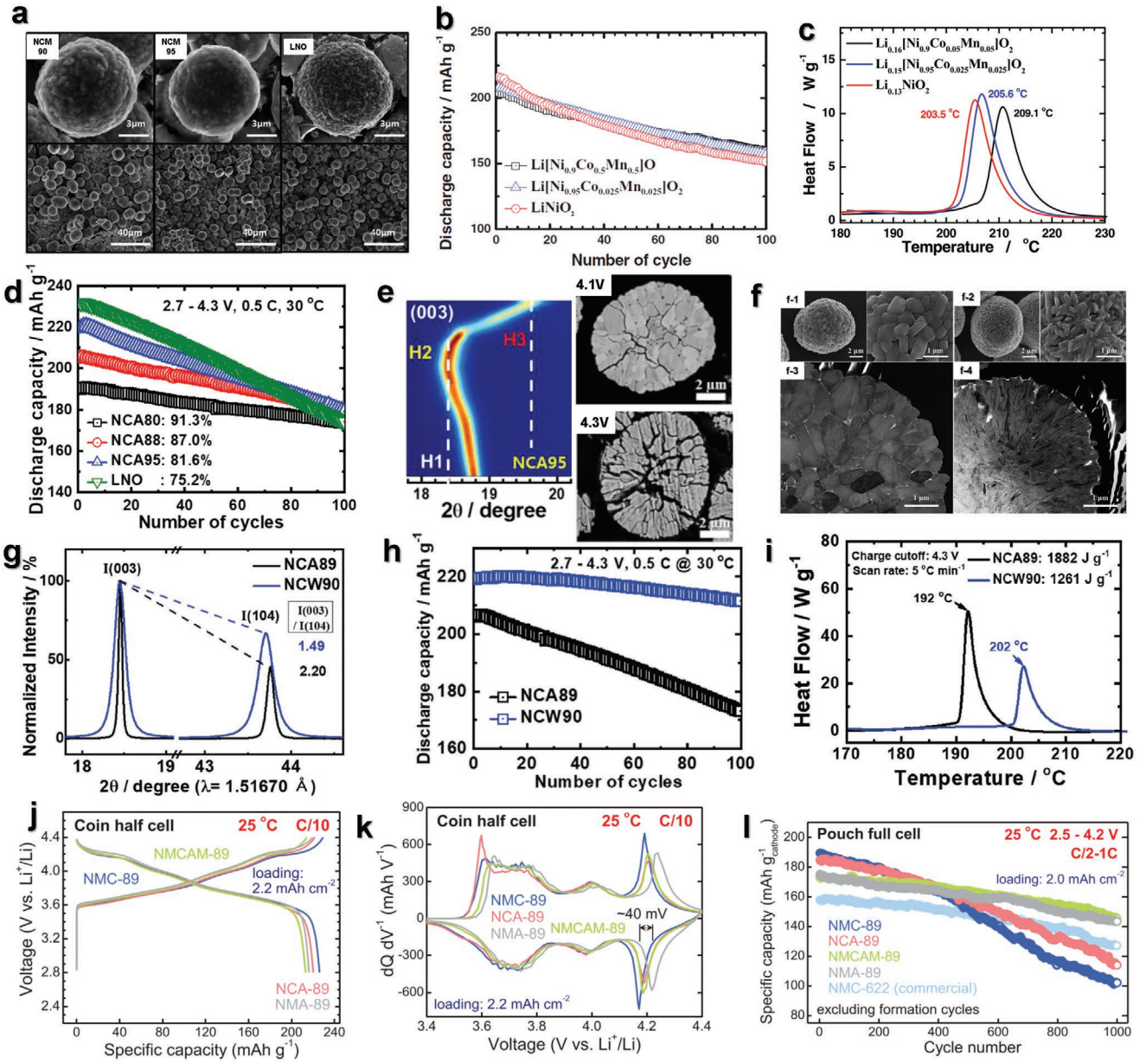

Figure 12. a) SEM images of as-prepared $Li[Ni_{0.9}Co_{0.05}Mn_{0.05}]O_2$, $Li[Ni_{0.95}Co_{0.025}Mn_{0.025}]O_2$, and $LiNiO_2$. b) Cycle retention of $Li[Ni_{1-x}Co_{x/2}Mn_{x/2}]O_2$ (x = 0.1, 0.05, 0) at a constant current density of 100 mA g^{-1} (0.5C) at 30 °C when cycled from 2.7 to 4.3 V. c) DSC profiles of the $Li[Ni_{0.90}Co_{0.05}Mn_{0.05}]O_2$, $Li[Ni_{0.95}Co_{0.025}Mn_{0.025}]O_2$, and $LiNiO_2$ electrodes with a scan rate 5 °C min^{-1}. The cells were charged to 4.3 V at a rate of 0.2C. Reproduced with permission.[89] Copyright 2015, The Electrochemical Society. d) Cycling performance at 0.5C (100 mA g^{-1}) at 30 °C. All cells were operated within a voltage range of 2.7–4.3 V. In situ XRD measurements of the NCA88 cathode during the first charge process. e) The contour plots of (003) Bragg reflection and comparison of cross-sectional SEM images of the NCA95 cathode under various SOCs (charged state at 4.1, and 4.3 V at initial cycle). Reproduced with permission.[70] Copyright 2019, American Chemical Society. f) SEM images at two different magnifications for NCA89 and NCW90 cathode particles. Bright-field STEM images show part of the particle cross-section for NCA89 and NCW90. g) Comparison of the two patterns after normalization with their (003) peak intensities. Comparison of the electrochemical performance of the NCA89 and NCW90 cathodes; h) cycling performance at 0.5C and 30 °C between 2.7 and 4.3 V using 2032 coin-type half-cells with a Li metal anode. i) DSC profiles for NCA89 and NCW90 in the delithiated state at 4.3 V. Reproduced with permission.[95] Copyright 2019, John Wiley and Sons. j) Charge–discharge voltage profiles at the fourth C/10 formation cycle, with cycling over 100 cycles at C/3 shown in the inset, k) $dQ\ dV^{-1}$ curves at the fourth C/10 formation cycle, l) long-term cycling over 1000 cycles at a C/2-1C charge–discharge rate. Reproduced with permission.[96] Copyright 2020, John Wiley and Sons.

Li_xNiO_2 electrodes charged to 4.3 V. The thermal stability was strongly dependent on the Ni composition; the high ratio of Co and Mn in the $Li_x[Ni_{0.90}Co_{0.05}Mn_{0.05}]O_2$ than that in $Li_x[Ni_{0.95}Co_{0.025}Mn_{0.025}]O_2$ and Li_xNiO_2 effectively reduced the thermal activity by shifting the onset temperature of the oxygen evolution toward a higher temperature region and reducing the heat released by the exothermic reaction.[89] $Li(Ni_{1-x-y}Co_xAl_y)O_2$ (NCA) is typically formulated to be Ni-rich with only a small

amount of Al.[90,91] Generally, NCA cathode materials crystallize in an O3-type structure (*R*-3*m*).[90,92] Repetitive de/lithiation leads to microcrack formation in the particles, leading to structural instability with poor cyclability. This phenomenon has been extensively investigated and resolved through additional processes, as discussed hereinafter. However, NCA has the advantage of combining the attractive properties of $LiNiO_2$ with those of $LiCoO_2$; thus, NCA has better structural stability than $LiNiO_2$ (Figure 12d).[70] Introduction of Co helps sustain the layered structure and provides reversible capacity with ≈91% retention compared to ≈75% retention for $LiNiO_2$. Additionally, the presence of electrochemically inactive Al^{3+} in the structure can induce structural stability at high potentials by preventing overcharging. Delmas and co-workers[93] reported that 15% Al content in $Li[Ni_{0.70}Co_{0.15}Al_{0.15}]O_2$ improved the capacity by ≈25 mAh g^{-1} compared with $Li_xNi_{0.89}Al_{0.16}O_2$. The irreversible capacity of ≈30 mAh g^{-1} for $Li[Ni_{0.70}Co_{0.15}Al_{0.15}]O_2$ was lower than that of $Li_xNi_{0.89}Al_{0.16}O_2$ (≈50 mAh g^{-1}), which was caused by the lower amount of Ni^{2+} in Li layers: <1% for $Li[Ni_{0.70}Co_{0.15}Al_{0.15}]O_2$ and 5% for $Li_xNi_{0.89}Al_{0.16}O_2$.[37] Indeed, the irreversible behavior derived from the high cation mixing ratio in the Li layer triggers local collapse of the layered structure, which hinders facile Li^+ diffusion and Li^+ deintercalation.[94] Therefore, $Li_x[Ni_{0.70}Co_{0.15}Al_{0.15}]O_2$ showed good reversibility with less dominant polarization during cycling. It is thought that the structural stability of $Li_x[Ni_{0.70}Co_{0.15}Al_{0.15}]O_2$ at the deep charged state arises from the suppression of overcharging.

However, the Co-less Ni-rich NCA95 structure suffered from severe capacity fading, which is correlated with the volume change caused by phase transition from H2 to H3 and the resulting formation of microcracks after charging to 3.9 V (Figure 12e). Therefore, suppressing or delaying the phase transition from H2 to H3 is an important method to improve the structural and chemical stability of Co-less Ni-rich NCA cathodes.

Double substitutions of Co^{3+} and W^{6+} into the $LiNiO_2$ cathode ($Li[Ni_{0.9}Co_{0.09}W_{0.01}]O_2$, NCW90) provided considerably improved cell performance than that of the $Li[Ni_{0.885}Co_{0.10}Al_{0.015}]O_2$ (NCA89) cathode.[95] As shown in Figure 12f-1,f-2, the NCA89 and NCW90 cathode materials prepared via coprecipitation comprised microspherical particles with an average diameter of 9–10 µm. The nanosized primary particles agglomerated to form secondary particles. The average size of the primary particles of NCA89 was ≈500 nm, whereas the average primary particles of NCW90 were elongated and much smaller, being less than ≈100 nm wide and ≈1 µm long. The difference in the internal microstructures of both cathode particles was clearly observed in bright-field scanning transmission electron microscopy images (Figure 12f-3,f-4). Relatively large and randomly oriented primary particles were agglomerated to form secondary particles in the NCA89 cathode, whereas relatively thin and elongated primary particles agglomerated to form the secondary particles in the NCW90 cathode. A lower $I_{(003)}/I_{(104)}$ peak ratio and higher degree of Li^+/Ni^{2+} cation mixing are observed for the NCW90 cathode than for the NCA89 cathode in Figure 12g. This is related to the increased Ni^{2+} content, which compensates for the charge imbalance. Furthermore, peak broadening of NCW90 was confirmed due to the relatively small particle size. The initial charge–discharge curves of the NCA89 and NCW90 cathodes were similar, with the first CE of ≈94% in the voltage range of 2.7–4.3 V at 0.1C at temperatures below 30 °C. For the NCW90 cathode, the first discharge capacity improved slightly to ≈231 mAh g^{-1} compared with ≈223 mAh g^{-1} for the NCA89 cathode. Notably, NCW90 showed high-power capability with an excellent cycle retention of ≈96% over 100 cycles, whereas the NCA89 cathode showed ≈83% retention (Figure 12h). The surface chemistry stabilized by the W-rich surface phase was notably reflected by the thermal stability of ternary Co-less Ni-rich $LiNiO_2$. The DSC results showed that the doping of the NC cathode with W effectively reduced the thermal activity by shifting the onset temperature of oxygen evolution toward a higher temperature region and reducing the heat released by the exothermic reaction (Figure 12i). The ternary Co-less Ni-rich cathodes with small amounts of Co, Al, and W overcame the issue of poor cyclability. More attention should be paid to further improve the structural and thermal stabilities of such cathodes. Recently, Manthiram and co-workers reported high nickel $LiNi_{1-x-y}Mn_xAl_yO_2$ (NMA) and Al–Mg-codoped NMC (NMCAM) with 89 % Ni content.[96] The initial discharge capacity of NMC-89, NCA-89, NMCAM-89, and NMA-89 were 226, 220, 213, and 216 mA h g^{-1} at 25 °C (Figure 12j) The tendency in specific capacities are related to properties of each metal ion, including redox reaction, oxidation state, and site occupancy. The observed trend follows Mg > Al > Mn > Co in reducing accessible capacities. Although NMA-89 showed the decreased discharge capacity, it shows a higher average operation voltage of nearly 40 mV than that of NMC-89 with good cyclability (Figure 12k,l).

4.2.2. Co-Less Ni-Rich NCMA and NCMW Cathodes

Of all the cathodes developed to date, Ni-rich layered NCM and NCA are the most promising, owing to their high reversible capacity and long cycling stability. The Ni content in both the cathodes has been progressively increased to enhance capacity and cost-effectiveness. Nevertheless, structural instability is always accompanied by a high content of Ni in Ni-rich NCM and NCA compounds. To overcome the obstacles posed by the increased Ni content, doping of the pristine NCM and NCA cathodes by "alien" transition metals has been attempted. Among the various dopants, Al is the most widely used because of its stabilizing role in the host-layered structure. The stability stems from the high bond strength of Al—O, compared to those of Ni—O, Co—O, and Mn—O. However, relatively low concentrations of the Al^{3+} dopant (below 5 mol%) are normally used for layered cathodes, owing to the inertness of Al. A 1.0 mol% Al-doped $Li[Ni_{0.90}Co_{0.05}Mn_{0.05}]O_2$ cathode (NCMA89) exhibited an improved cell performance with a longer cycle life than $Li[Ni_{0.885}Co_{0.100}Al_{0.015}]O_2$ (NCA89) and $Li[Ni_{0.900}Co_{0.05}Mn_{0.05}]O_2$ (NCM90).[97] **Figure 13**a shows that the difference in capacity between NCMA89 and NCM89 is insignificant (228 and 229 mAh g^{-1}, respectively) because of the negligible amount of Al in the compound. Meanwhile, the NCMA89 cathode showed improved cyclability over 100 cycles at 0.5C (90 mA g^{-1}), not only between 2.7 and 4.3 V (Figure 13b), but also at the upper cutoff voltage of 4.5 V (Figure 13c). This improvement is caused

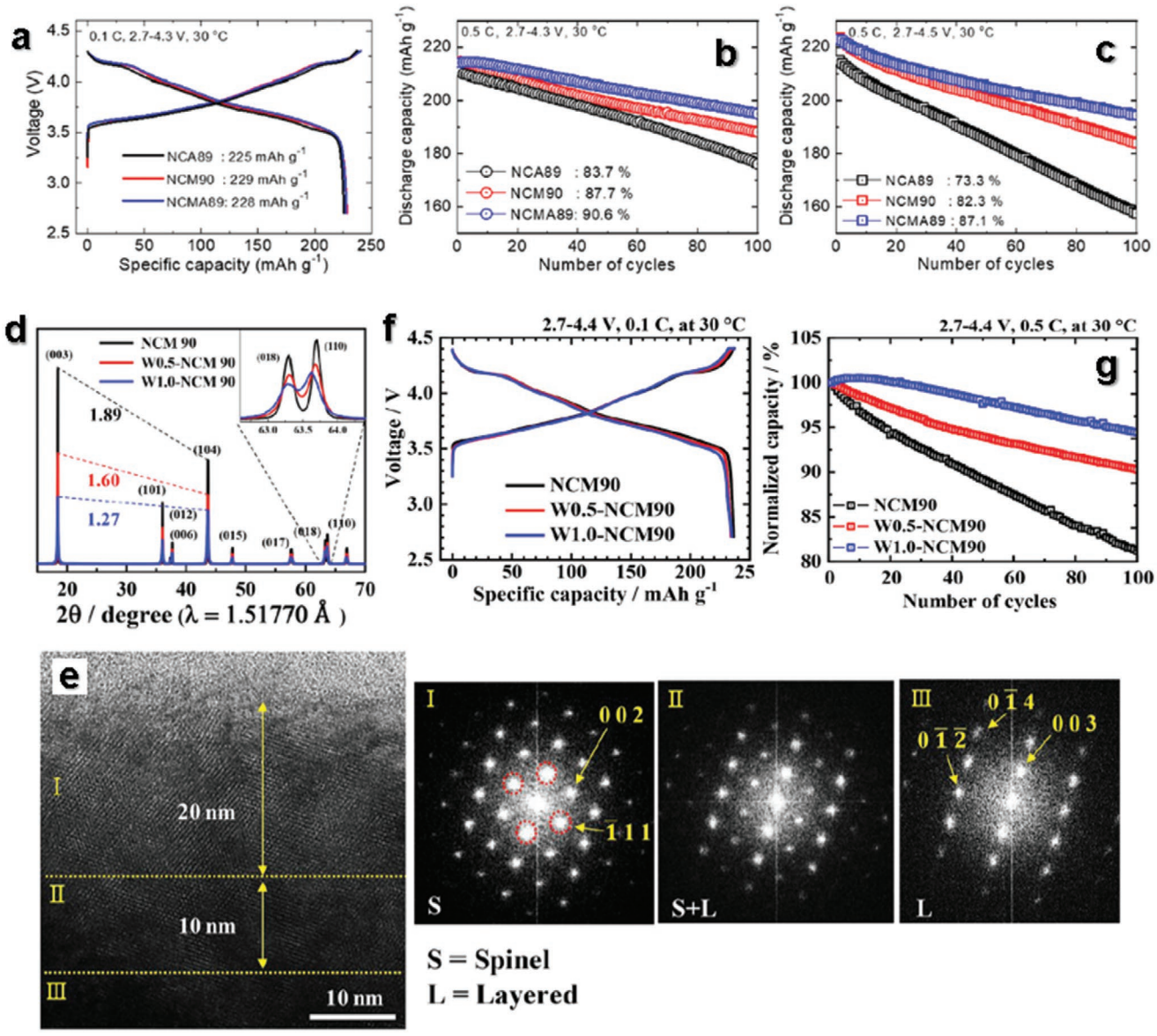

Figure 13. Comparison of the electrochemical performance of the NCA89, NCM90, and NCMA89 cathodes: a) first cycle voltage profiles for the three cathodes. All cells were cycled in the voltage range of 2.7–4.3 V at 0.1C and 30 °C in a half-cell using Li metal as an anode. Cycling performance of the three cathodes in the voltage range of b) 2.7–4.3 and c) 2.7–4.5 V at 0.5C and 30 °C. Reproduced with permission.[97] Copyright 2019, American Chemical Society. d) XRD patterns and (003)/(104) intensity ratios of the as-prepared NCM90, W0.5-NCM90, and W1.0-NCM90. e) High-resolution TEM images of textured primary particle surface and FT images (marked as I, II, and III) for as-prepared W1.0-NCM. f) Initial charge/discharge voltage profiles and g) cycle performance at 2.7–4.4 V for the NCM90, W0.5-NCM90, and W1.0-NCM90 cathodes. Reproduced with permission.[98] Copyright 2019, Elsevier.

by the contribution of the Al dopant, which substantially influences the structural stability by sharing the oxygen ions of AlO_6 with those of MO_6 (M: Ni, Co, and Mn) in the transition metal layers. Thus, the reduced movement of the *c*-axis played a crucial role in delaying the structural change from H2 to H3 in a highly delithiated state, enabling high capacity delivery over cycling. The presence of W^{6+} in some of the transition metal sites leads to the formation of Ni^{2+} to achieve charge balance in the Li layers because of the similarity in ionic radii.[98] This agrees with the decreased $I_{(003)}/I_{(104)}$ peak ratio and the higher degree of Li^+/Ni^{2+} cation mixing in the as-prepared 1 mol% W-doped $Li[Ni_{0.90}Co_{0.05}Mn_{0.05}]O_2$ (W1.0-NCM) (Figure 13d). Note that the W dopant modified the particle surface by forming a 20 nm thick spinel-like phase (Figure 13e). This acted as a buffer, effectively protecting the particle surface from attack by the electrolyte during extensive cycling. In these cation-intermixed cathodes, the secondary spinel-like phase that was formed on the primary particle surface induced enhanced structural stability. The stability was further attributed to the reduced H2 ↔ H3 phase transition, which suppressed the formation of detrimental microcracks observed with Al doping. Although the first discharge capacity declined slightly with an increase in the content of W present in the structure in the voltage range of 2.7–4.4 V at 0.1C (18 mA g^{-1}) at 30 °C

(Figure 13f), the cyclability for 100 cycles at 0.5C (90 mA g^{-1}) was effectively improved (Figure 13g). In addition to Al or W dopants, the introduction of Na^{+},[99] Mg^{2+},[100] and Zr^{4+}[101] into the NCM cathode may suppress microcrack formation and ensure long cycle life due to their pillar effect. Therefore, quaternary Co-less Ni-rich Ni–Co–Mn–M (Al^{3+}, W^{6+}) exhibited structural stability, owing to the decrease in volume expansion. To further increase the discharge capacity, introduction of more redox pairs, such as $Fe^{3+/4+}$ and $V^{3+/4+}$, is essential.

As mentioned before, the particles of the Ni-rich cathode materials suffered from severe structural degradation caused by highly deleterious oxygen loss, multiphase transition, and the development of severe microcracks from the inner core. To further develop Ni-rich cathode materials with better structural and electrochemical properties, various transition metal ions have been doped into the Ni–Co–Mn-based cathode materials. In particular, Al and W-doping provided enhanced structural stability in the NCM system. This is caused by the strength of the Al—O bond and the decrease in the particle size with increasing Al and W content. Major and co-workers elucidated the effects of Al doping on the electrochemical properties of the NCM system with the aid of theoretical predictions.[102] Considering all of the possible doping sites, the most energetically favorable structure was predicted to be stoichiometric $Li[Ni_{0.45}Co_{0.2}Mn_{0.3}Al_{0.05}]O_2$ with Al substitution for Ni in each transition metal layer, as shown in **Figure 14**a. The predicted formation energies of various compositions in the partially delithiated state suggested that Al-doped NCM-523 has a higher negative formation energy, which suggests a solid solution reaction. This means that Al-doped NCM-523 was more stable than undoped NCM-523 (Figure 14b). Li^{+} diffusion occurs primarily via an oxygen dumbbell hops pathway, and it was predicted that a Li^{+} diffusion

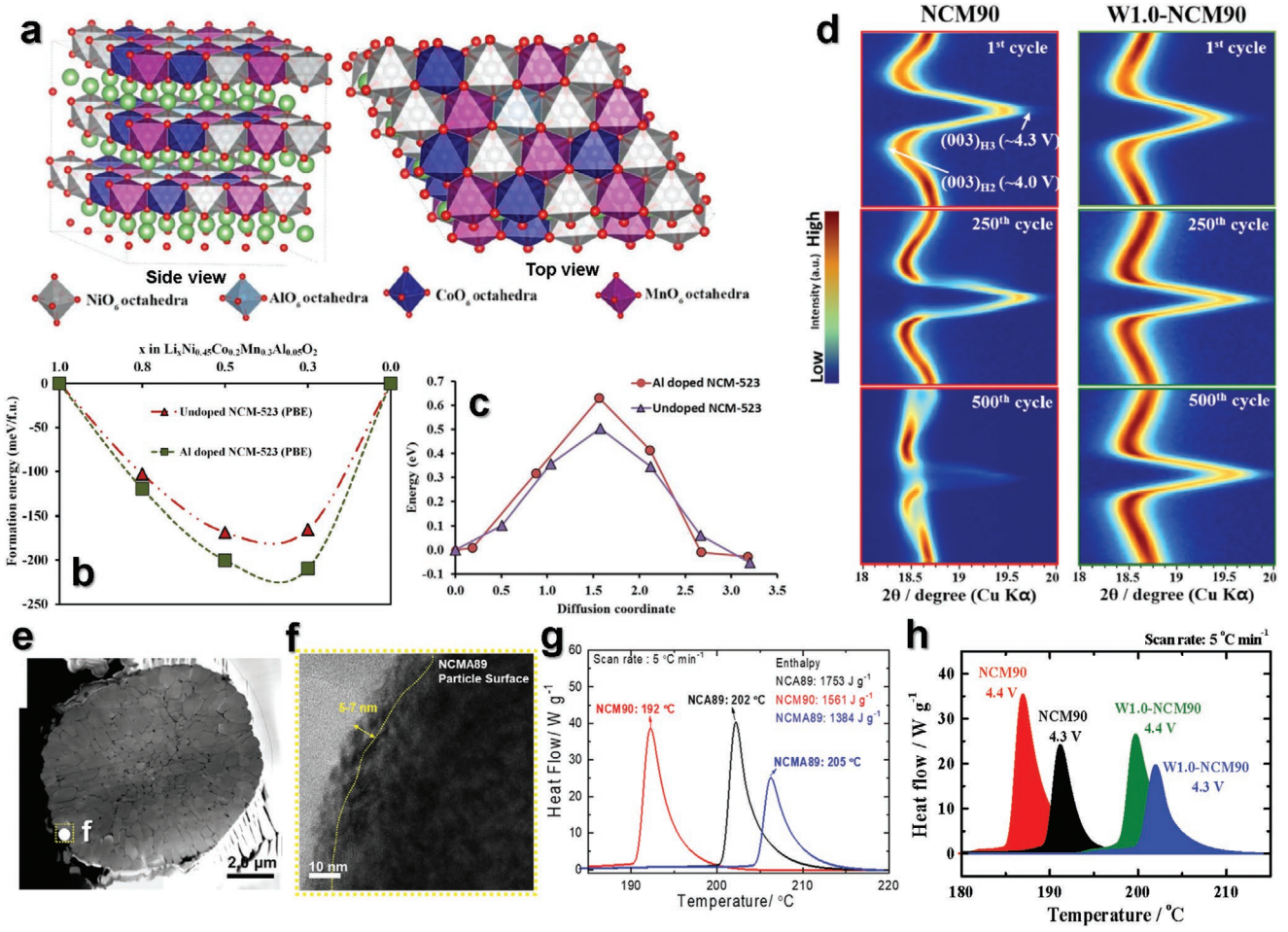

Figure 14. a) Relaxed supercell of $LiNi_{0.45}Co_{0.2}Mn_{0.3}Al_{0.05}O_2$, side-view of the supercell, and top-view of the supercell showing the cation ordering. Li atoms are shown as green spheres. b) Calculated formation energies of Al-doped and undoped NCM-523 using the PBE method. c) Li diffusion profile of the undoped and Al-doped NCM-523 using PBE; NEB energy profile. Reproduced with permission.[102] Copyright 2017, The Electrochemical Society. d) Contour plots for selected 2θ ranges corresponding to the (003) reflection of the cycled NCM90 and W1.0-NCM90 full cells. Reproduced with permission.[98] Copyright 2019, Elsevier. Mosaic scanning TEM images of the cycled cathodes after 100 cycles: e) NCMA89. High-resolution TEM images of surface primary particles: f) NCMA89 cathodes after 100 cycles. The high-resolution TEM images in (f) correspond to the regions marked by yellow boxes in (e). g) DSC profiles for the NCA89, NCM90, and NCMA89 cathodes measured in their second charged state ($Li_{0.3}MO_2$) in the presence of 1.2 M $LiPF_6$ EC:EMC = 3:7 by vol% with 2 wt% VC. Reproduced with permission.[97] Copyright 2019, American Chemical Society. h) DSC results of NCM90 and W1.0-NCM90 charged to 4.3 and 4.4 V together with the electrolyte solution of 1.2 M of $LiPF_6$, EC/EMC (3:7 v:v), and 2 wt% VC. Reproduced with permission.[98] Copyright 2019, Elsevier.

barrier of ≈0.50 eV must be overcome for Li^+ diffusion to occur within the undoped NCM-523 structure (Figure 14c). The Li^+ diffusion barrier for the Al-doped NCM-523 structure was slightly higher at ≈0.63 eV, indicating the mitigation of Li^+ diffusion. In general, the lattice changes of Al-doped and undoped samples are similar in the delithiated state.[103] The increase in the Li^+ diffusion barrier is related to local effects that do not affect the Li^+ diffusion rates. Thus, NCMA cathode materials can deliver high reversible capacity with long-term cycle life.[97] As mentioned before, the primary particle size, which was decreased by W-doping, influences the suppression of severe microcrack propagation from the inner core. Furthermore, W-doping modified the particle surface of the NCM system by forming a spinel-like phase as a buffer, which effectively protects the particle surface from chemical attacks by the electrolyte during extensive cycling (Figure 13e).[98]

Based on these effects, W1.0-NCM showed structural stability, and the generation of internal strain accompanied by microcracks and phase transition from H2 to H3 were suppressed even after 500 cycles (Figure 14d).[98] Because of these excellent properties of the NCMA and NCMW electrodes, despite having an upper cutoff voltage of 4.4–4.5 V, these electrodes are more promising for the industrial development of EVs which require a high energy density with a long battery life compared with the counterparts substituted with other transition metals. Notably, no formation of microcracks was observed as a result of the structural stability of the surface rocksalt layer with a thickness of 5–10 nm (Figure 14e,f).[97] In addition, the onset temperature of oxygen evolution and the heat released during the exothermic reaction could be reflected by effective doping of Co, Mn, Al,[97] and W[98] in quaternary Co-less Ni-rich $LiNiO_2$ (Figure 14g,h). Numerous challenges still exist, such as surface residual lithium compound generation and the side reaction with the electrolyte, which may lead to deteriorative cycling performance. Advanced surface modification methods stated in Section 3.2 can provide possible solutions to not only retain the high capacity for a long term but also raise the temperature of exothermic decomposition to an elevated level.

4.3. Compositionally and Structurally Designed Co-Less Ni-Rich Layered Cathodes

4.3.1. From Core–Shell (CS) to Hybrid Structure

Although surface modification can enhance the structural stability of Ni-rich cathode materials, it is difficult to homogeneously encapsulate the surface of active materials with thin layers. Most importantly, surface modification cannot completely control the inner side of the materials. Therefore, compositionally and structurally designed Ni-rich layered cathodes were introduced to satisfy the requirements of high capacity and enhanced safety of Ni-rich cathode materials. The material design has sequentially progressed through four steps, i.e., CS in 2006,[104] core–shell concentration gradient (CSG) in 2009,[105] and full concentration gradient (FCG) in 2012[106] (**Figure 15**), as well as the advanced full concentration gradient with two slope (TSFCG) in 2015.[107] These strategies enabled the development of cathodes for LIBs with improved structural stability and safety. In the first reported CS-$Li[(Ni_{0.8}Co_{0.1}Mn_{0.1})_{0.8}(Ni_{0.5}Mn_{0.5})_{0.2}]O_2$, the spherical morphology of the hydroxide was completely maintained after calcination at a high temperature (Figure 15a).[104] The $Li[Ni_{0.8}Co_{0.1}Mn_{0.1}]O_2$ delivered a high discharge capacity but poor capacity retention. The CS $Li[(Ni_{0.8}Co_{0.1}Mn_{0.1})_{0.8}(Ni_{0.5}Mn_{0.5})_{0.2}]O_2$, which was formed between the Ni-rich $Li[Ni_{0.8}Co_{0.1}Mn_{0.1}]O_2$ core and the Mn-rich $Li[Ni_{0.5}Mn_{0.5}]O_2$ shell, showed excellent long-term cycle life, which is attributed to the structural stability. This is caused by the presence of Mn^{4+} in the $Li[Ni_{0.5}Mn_{0.5}]O_2$ shell. Next, the CS-$Li[Ni_{0.95}Co_{0.025}Mn_{0.025}]O_2$ cathode was developed to elongate the nanoscale primary particles in a compact manner along the radial direction in contrast to with previously reported $LiNiO_2$ cathodes with aggregated randomly oriented particles.[89] In particular, the Ni-depleted shell provided remarkably improved capacity retention which exceeded that of unmodified $LiNiO_2$ (Figure 15b).[108] However, structural mismatch between the core and shell was observed at a deeply delithiated state, which was not suitable for long-term cycling.[109] The mismatch is mainly attributed to the variation in the *c*-axis at the charged state due to the different *c*-axis parameters of the $Li_{1-x}[Ni_{0.8}Co_{0.1}Mn_{0.1}]O_2$ core and $Li_{1-x}[Ni_{0.5}Mn_{0.5}]O_2$ shell. As the next step, the CSG, in which a concentration gradient of transition metals was formed in the shell part, was introduced to overcome the problem of the structural mismatch between the core and the shell. Thus, the CSG material was designed to exhibit hybridized morphological and electrochemical properties, in which the high discharge capacity was related to the Ni-rich core, and the long-term cycle life and safety were derived from the Mn-rich outer shell (Figure 15c,d).[110] According to the design, the CSG was effective in improving the cyclability by mitigating the difference in the variation in the *c*-axis lattice parameters during de/lithiation. The concentration gradient was further changed from the core to the surface of the spherical particles, i.e., an FCG-type layered compound with continual variation of the concentration gradient of transition metals from the center toward the outer layer was fabricated (Figure 15e).[106] The FCG-$Li[Ni_{0.60}Co_{0.15}Mn_{0.25}]O_2$ showed a high discharge capacity of 206 mAh g^{-1} at a 0.5C-rate in the voltage range of 2.7–4.5 V and enhancement of the capacity retention to ≈90.7% from ≈82.8% for conventional $Li[Ni_{0.60}Co_{0.15}Mn_{0.25}]O_2$ (Figure 15f). This is associated with the variation in the composition of the transition metal ions from the core to the outer layer. Thus, Ni provided high capacity and energy density, which gradually increased from the outer layer to the center, whereas Mn, which provided structural stability, was present in the inner central region (single slope). To further improve the morphology, the FCG type sample was modified to microspherical particles with rod-shaped primary particles that were oriented from the particle center (Figure 15g,h).[107] To further extend this compositional and structural design, advanced TSFCG cathodes were proposed.[111,112] The TSFCG cathodes with concentration gradients of Ni and Mn displayed an excellent power capability of ≈210 mAh g^{-1}, with a capacity retention of ≈93% over 100 cycles (Figure 15h). Although these compositional gradation strategies such as CS, CSG, FCG, and TSFCG are widely recognized to be practical for Ni-rich cathodes with Ni content between 60% and 90%, more efforts are required to further increase the Ni content (≥95%)

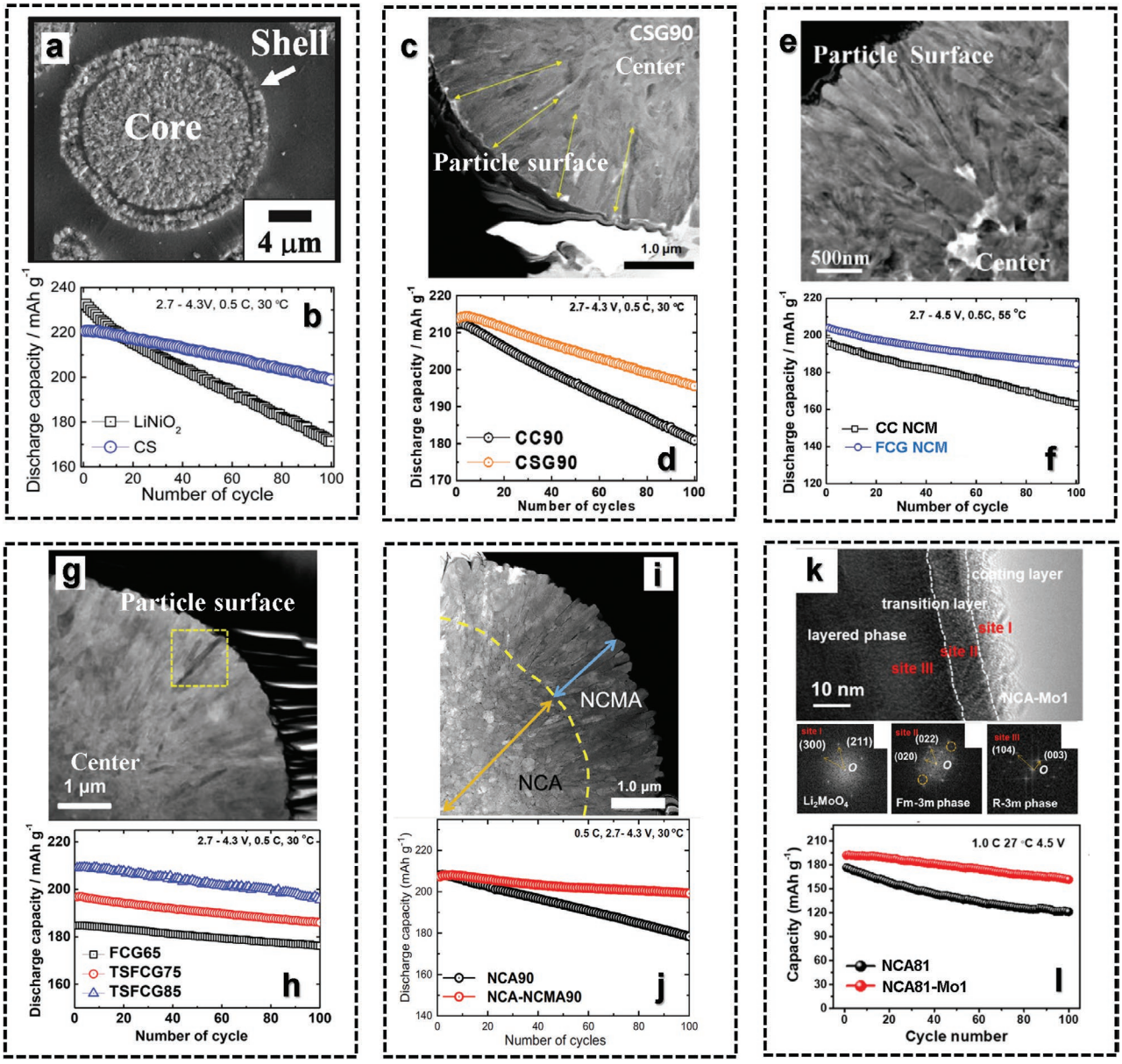

Figure 15. CS particle evolution stages: a) CS $Li[(Ni_{0.8}Co_{0.1}Mn_{0.1})_{0.8}(Ni_{0.5}Mn_{0.5})_{0.2}]O_2$ and discharge capacity versus cycling number plots of C/$Li[Ni_{0.8}Co_{0.1}Mn_{0.1}]O_2$ and C/$Li[(Ni_{0.8}Co_{0.1}Mn_{0.1})_{0.8}(Ni_{0.5}Mn_{0.5})_{0.2}]O_2$ cells. (*x*: capacity, *N*: cycling number). Reproduced with permission.[104] Copyright 2006, The Electrochemical Society. b) SEM images of CSG of $Li[Ni_{0.64}Co_{0.18}Mn_{0.18}]O_2$ and cycling performance of half-cells based on $Li[Ni_{0.8}Co_{0.1}Mn_{0.1}]O_2$ and $Li[Ni_{0.46}Co_{0.23}Mn_{0.31}]O_2$, and concentration gradient material cycled between 3.0 and 4.4 V at 55 °C by applying a constant current at a rate of 0.5C (95 mA g^{-1}). Reproduced with permission.[108] Copyright 2017, American Chemical Society. c) Bright-field TEM image; CSG90. d) Cycling performances at 0.5C of CC90 and CSG90. Reproduced with permission.[110] Copyright 2019, John Wiley and Sons. e) Cross-sectional TEM image of a single FCG–Mn–F particle, f) cycling performance of half-cells between 2.7 and 4.5 V at 55 °C by applying a constant current rate of 0.5C (114 mA g^{-1}). Reproduced with permission.[106] Copyright 2013, American Chemical Society. g) Bright-field TEM images of TSFCG 85, and h) cycling performance at 0.5C (90 mA g^{-1}) at 30 °C. All cells were operated within a voltage range of 2.7–4.3 V. Reproduced with permission.[107] Copyright 2017, American Chemical Society. The blue dashed line indicates the particle center, and the orange dashed line indicates particle core. The Ni-rich NCA particle center and the Mn-rich NCMA outer surface are clearly revealed by the EPMA line-scans; i) dark-field TEM image. The NCA–NCMA90 cathode outperforms the conventional NCA90 cathode in terms of cycling stability. Cycling performance of the cathodes in the voltage ranges of j) 2.7–4.3 V at 0.5C and 30 °C in half-cells with Li metal anode. Reproduced with permission.[113] Copyright 2019, Elsevier. k) HRTEM image of NCA-Mo1 sample and SAED patterns for NCA-Mo1 at site I, II, and III. l) Cycling performance for NCA-0 and NCA-Mo1 at a high cut-off cell potential. Reproduced with permission.[114] Copyright 2019, American Chemical Society.

as they require an excessively steep concentration gradients at the particle periphery. To overcome the inherent structural instability of Ni-rich cathodes, Sun and co-workers proposed a hybrid NCA–NCM cathode, $Li[Ni_{0.886}Co_{0.049}Mn_{0.050}Al_{0.015}]O_2$, composed of a Ni-rich NCA core encapsulated by a 1 μm thick Al-doped NCM shell (Figure 15i).[113] The proposed hybrid NCA–NCM cathode could exhibit stable capacity retention with a significant increase in the capacity during extensive cycling

(Figure 15j), even at a high cutoff voltage of 4.5 V and a temperature of 45 °C.[113] The remarkable long-term cycling stability was associated with cation ordering between Li and the transition metal ions, similar to the Zr-doped $LiNiO_2$ cathode.[39] The $Li[Ni_{0.5}Mn_{0.5}]O_2$ layer with a microscale thickness covering the high capacity $Li[Ni_{0.8}Co_{0.1}Mn_{0.1}]O_2$ was a challenge to fully utilize the capacity provided by $Li[Ni_{0.8}Co_{0.1}Mn_{0.1}]O_2$ and protect the active material with stable $Li[Ni_{0.5}Mn_{0.5}]O_2$. The progressive evolution to CSG, FCG, and TSFCG demonstrate the remarkable improvement and advances in powder technologies that have optimized electrode performances with high capacity for long term and acceptable thermal stability. Further work should be directed toward enforcement of the particle strength to extend the durability of Ni-rich NCM compounds. This may provide insights into the complex reaction mechanisms between the electrolyte and surface/internal structure of the electrode, thus suppressing the decay of electrode as well as electrolyte decomposition at especially high voltage.

Further, Xu et al. investigated that Ni-rich NCA ($LiNi_{0.815}Co_{0.15}Al_{0.035}O_2$) cathode with 1% Mo^{6+} induced epitaxially grown nanostructured hybrid surface as a surficial gradient concept which is different from structural gradients like CSG, FCG, and TSFCG.[114] According to the microstructural information in Figure 15k, it the surface of NCA-Mo1 particle is epitaxially separated from the surface to bulk that they are interfaced with the transition layer; namely, the shell (Li_2MoO_4), the transition phase (rocksalt NiO, *Fm*-3*m*), and the bulkcore (*R*3-*m*).[114] The cycling performance showed discharge capacities of ≈180 and ≈190 mAh g^{-1} for NCA-0 and NCA-Mo1, respectively, in the range of 2.7–4.5 V at 1C. Compared with the NCA-0 that suffered from capacity fading, the NCA-Mo1 delivered stable cycling performance with a capacity of 162.0 mAh g^{-1}, corresponding to the capacity retention of 84.5% after 100 cycles (Figure 15l).[114]

4.3.2. To Better Bulk and Interphase Stability

Spherical CS structured $Li[Ni_{0.95}Co_{0.025}Mn_{0.025}]O_2$ exhibits improved cyclability with a capacity retention of ≈90% over 100 cycles, compared with that of $LiNiO_2$ (Figure 15b). This was due to the well-preserved compositional partitioning even after 100 cycles caused by the CS structure (**Figure 16**a).[108] The HRTEM images of the [010] zone with Fourier transform of the image verified that a 20 nm thick rock salt structure (*Fm*-3*m*) was formed along the edge of the primary particle (Figure 16b).[108] Capacity fading of the Ni-rich cathodes with a Ni content of ≥80% was mainly caused by phase transition from H2 to H3, leading to severe crack formation, associated with the two different phases (between the surface and bulk structure) in the CSG90 cathode, as shown in Figure 16c.[110] The radial texturing of the primary particles in the shell can dissipate the internal strain and microcrack formation in the deeply delithiated state, thereby suppressing electrolyte penetration into the bulk of the particles, whereas severe formation of the NiO-like rock salt structure was observed only on the cracked surface of inferior particles. Although the CSG structure affords improved structural and electrochemical stability, it still suffers from different levels of lattice volume variation because of the void layer formed at the interface between the core and shell after extensive cycling.[109] In fact, the compositionally and structurally designed Ni-rich layered cathode materials showed relatively enhanced structural and chemical stability. In particular, the FCG structure with continual variation of the concentration of transition metal ions from the inner core to the outer layer of the particle showed improved capacity due to the Ni-rich core and structural and thermal stability of the Mn-rich outer layer (Figure 16d).[115,116] Furthermore, strong crystallographic texturing was developed on the rod-shaped primary particles, along with highly correlated particle orientation in the advanced FCG with the two slope Ni-rich NCM cathode (Figure 16e).[107] This unique morphology made it possible to reduce the anisotropic internal strain induced by removing Li from the Ni-rich NCM cathodes and enabled the high rate cycling by facilitating Li^+ diffusion by providing fast diffusion pathways. In contrast, the deeply delithiated NCA82 sample showed severe structural degradation due to electrolyte penetration into the particle interior at elevated temperatures. In addition to the normal compositional gradation strategies, a hybrid NCA NCMA cathode was proposed as a Ni-rich cathode with high Ni content, which provided microstructural stability with ordered intermixing of Li and the transition metal ions. This cation ordering stabilized the host structure upon extensive cycling and facilitated Li intercalation. The effect of the hybrid structure was clearly observed because the full cell when paired with graphite maintained ≈95% of its initial capacity even after 1000 cycles.

As another strategy, 1% Mo-modified $LiNi_{0.815}Co_{0.15}Al_{0.035}O_2$ (NCA-Mo1) cathode, was introduced by a wet-chemical coating of NCA with $(NH_4)_2MoO_4$ as the coating precursor. The introduction of Mo^{6+} ions not only reduced residual lithium compounds to form conducting Li_2MoO_4 coating layer on the surface of NCA but also rendered to form an epitaxially grown NiO rocksalt phase in the surface region for the Ni^{2+} reduced from Ni^{3+} after the Mo^{6+} incorporation into the core direction. Therefore, the Mo-modified Ni-rich cathode material demonstrates an architecture of epitaxially grown nanostructured hybrid surface consisting of Li_2MoO_4, NiO-like phase (*Fm*-3*m*), and layered structure (*R*-3*m*) with Mo gradient concentration to the core from the shell (Figure 16g).[114]

In comparison, TSFCG cathodes and the hybrid NCA–NCMA cathode had the most stable structural and electrochemical properties among the Ni-rich cathode materials, as illustrated in **Figure 17**. W is also found to be the best dopant for Ni-rich cathodes (such as W1.0-NCM90 and NCW90) for developing advanced cathode materials for LIBs. Considering the commercialization and cost-effectiveness for industry, the compositional and structural co-precipitation design method is preferable because of its ease of scale-up for the industry, as well as the low cost of lab-scale operation. Therefore, advanced engineering using mixed strategies for coating and concentration gradients for bulk and interphase stability will be required in the future.

4.3.3. Improved Thermal Stability

With increasing temperature, the surface structures grow toward the core, and the near-surface rock salt

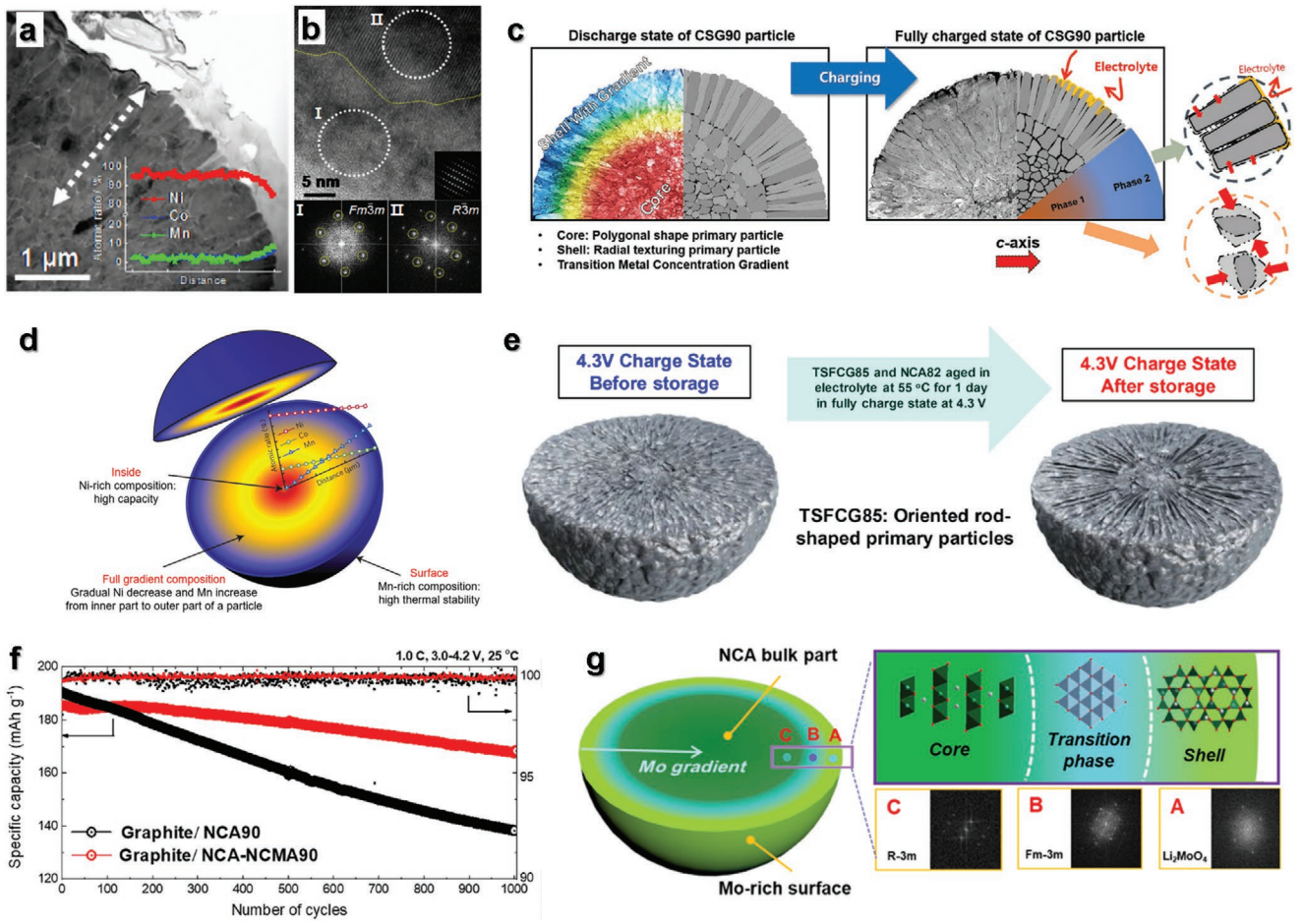

Figure 16. a) EDS compositional line-scan of a particle from the cycled CS cathode after 100 cycles, and b) high-resolution TEM image of the cycled CS cathode with Fourier transform from regions marked I and II. Schematic description of the discharged and charged states. Reproduced with permission.[108] Copyright 2017, American Chemical Society. Schematic description of the discharged and charged states. c) CSG90 cathode showing the internal morphological difference and the sustained damage. Reproduced with permission.[110] Copyright 2019, John Wiley and Sons. d) Schematic diagram of the FCG lithium transition-metal oxide particle with the nickel concentration decreasing from the center toward the outer layer and the concentration of manganese increasing accordingly. Reproduced with permission.[115] Copyright 2012, Macmillan Publishers Limited. e) Schematic representation of the high-temperature aged TSFCG85 cathodes showing the internal morphological difference and the sustained damage. Reproduced with permission.[107] Copyright: American Chemical Society 2017. f) Long-term cycling performance of the NCA90 and NCA–NCMA90 cathodes in full cells. Reproduced with permission.[113] Copyright 2019, Elsevier. g) Schematic diagram of a Mo-modified $LiNi_{0.815}Co_{0.15}Al_{0.035}O_2$ cathode material. Reproduced with permission.[114] Copyright: American Chemical Society 2019.

structure gradually increases. To prevent this severe structural change, many researchers have investigated and developed various types of Ni-rich cathode materials through effective doping, surface modification, and gradient strategies, as summarized in **Figure 18** and **Table 4**. Commonly, the Ni-rich cathode materials, $Li[Ni_{0.84}Co_{0.06}Mn_{0.09}Al_{0.01}]O_2$ (TSFCG-Al), $Li[Ni_{0.5}Mn_{0.5}]O_2$, $Li[Ni_{0.9}Mn_{0.1}]O_2$, CS-$Li[(Ni_{0.8}Co_{0.1}Mn_{0.1})_{0.8}(Ni_{0.5}Mn_{0.5})_{0.2}]O_2$, $Li[Ni_{0.60}Co_{0.15}Mn_{0.25}]O_2$ (FCG65), and $Li[Ni_{0.60}Co_{0.15}Mn_{0.25}]O_2$ (CC NCM), with a Mn ratio of over 0.09 exhibit thermal stability with a relatively high-temperature exothermic peak (over 250 °C). Thus, the Ni-rich cathode materials should be doped with not only Mn for enhanced safety but also with a small amount of other transition metals (Co, Mn, Al, and W) to enhance the thermal properties. Furthermore, the interphase stability between the electrode and electrolyte achieved via compositional and structural design by gradually decreasing the Ni concentration from the inner core to the outer layer is beneficial for improving the thermal stability. It was demonstrated that Ni-rich cathode materials to which compositional gradation strategies such as CS, CSG, FCG, and TSFCG are applied provide a commercialization possibility by resolving the issues related to thermal safety and poor cyclability of $LiNiO_2$. Furthermore, the surface modification is an effective skill for improvement of thermal stability by preventing the direct contact between the electrode and electrolyte. This is closely related to the performance of the final product of Ni-rich cathodes. Although the surface modification technologies for Ni-based cathodes with a Ni content of under 80% have been developed, technologies for surface modifications of Ni-based cathodes with a Ni content of over 90% have not been developed yet. Therefore, the development of surface modification skills suitable for Ni-rich cathode materials is urgently required for thermal stability.

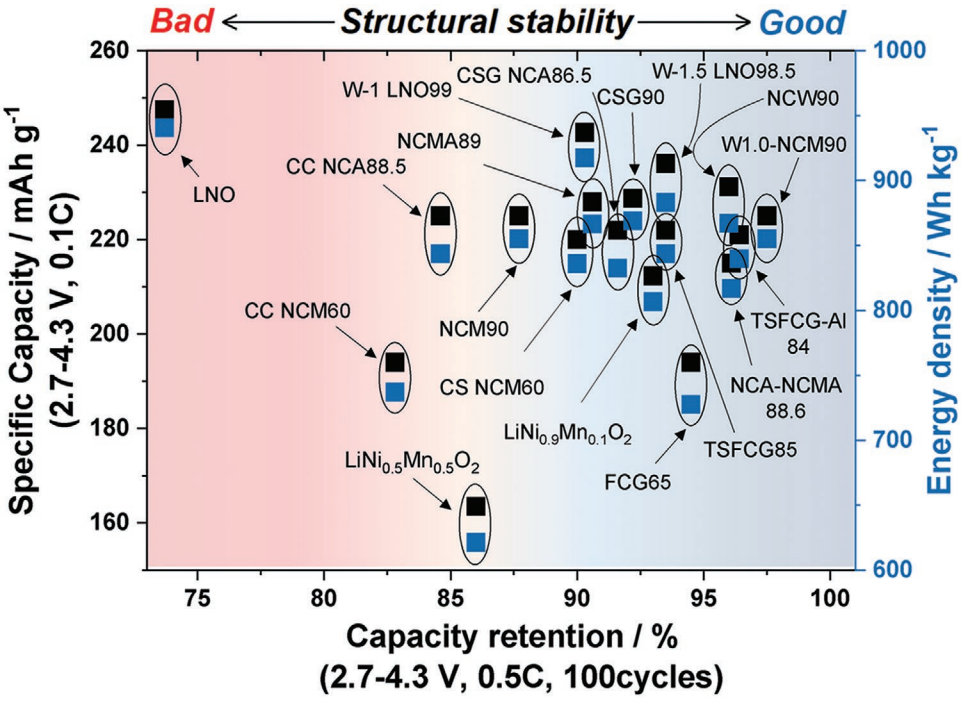

Figure 17. Comparison of the structural stability of the different Ni-rich cathode materials.

5. Conclusions and Outlook

Ni-rich layered compounds with high energy densities and low costs have been receiving increasing attention as promising cathode candidates for next-generation EVs. However, the application of these cathodes to commercial products is still challenging because of their structural and thermal instabilities. In particular, in nickel-based cathodes with an Ni content of ≥80%, multistep phase transition leads to microcrack formation in the particles, thus deteriorating the electrode performance. Furthermore, the release of oxygen poses a risk of battery explosion and is a security hazard of battery use. This thermal runaway mechanism is related to the structural instability. These problems can be addressed by applying advanced techniques to $LiNiO_2$.

In this review, we discussed the achievements and strategies for improving the overall performance of Co-less Ni-rich layered oxide cathode materials for LIBs, and the results are summarized in **Figure 19**. Doping as a novel strategy for improving the properties may be very helpful in maintaining the structural stability and enhancing the stability by strengthening the lattice interactions between the transition metal and oxygen. This technique also plays an important role in enhancing the thermal stability of the Ni-rich layered oxides by suppressing the formation of the spinel phase, which leads to drastic capacity fading. Especially, a low percent of substitutions (<3 wt%) with elements such as Mn, Mg, Al, Zr, and Ti help maintain the structural stability of materials almost without sacrificing the specific capacity and energy density.

Another critical concern of Ni-rich materials is the surface chemistry. The side reactions of Ni4+ with the electrolyte at a highly delithiated state lead to the formation various side products. The HF attack from electrolyte degradation by water causes phase transformation, transition metal dissolution, and structural damage to the outer layer of the electrode. Therefore, uniform protective layers coatings, which can prevent such types of degradation, are important. The development of electrolytes with functional additives is highly sought-after and anticipated for the realization of long-cycling stability of LIBs based on the Ni-rich cathodes. Such additives can not only help stabilize the Ni-rich cathode–electrolyte interface but also alleviate gas generation. The unwanted side reactions between the electrode and electrolyte can be significantly mitigated through surface modifications. Understanding not only the surface chemistry but also the chemistry of the inner side is required to perfect the design of cathode materials with excellent overall performance.

The concept of the compositional gradient approach in Ni-rich materials has been developed and has shown superiority under extensive cycling compared to regular NCA and NCM with a similar composition of Ni. Obviously, quaternary Co-less Ni-rich cathode materials such as NCMA89 and compositionally and structurally designed Co-less Ni-rich layered cathodes such as TSFCG85 and TSFCG–Al show promising structural, electrochemical, and thermal stabilities properties among the Ni-rich cathode materials. Together with the improved thermal stability and additional surface layer treatment, the concentration gradient method can provide a viable solution to satisfy the requirements of commercial cathode materials for future EVs. Therefore, they may be the best candidates Co-less Ni-rich cathode materials to resolve the problems related to structural instability, capacity degradation, and safety concerns with prospective improvements in cost.

More attention should be paid to advance robust engineering to further enhance the overall properties, even under severe battery operating conditions. Therefore, advanced next-generation

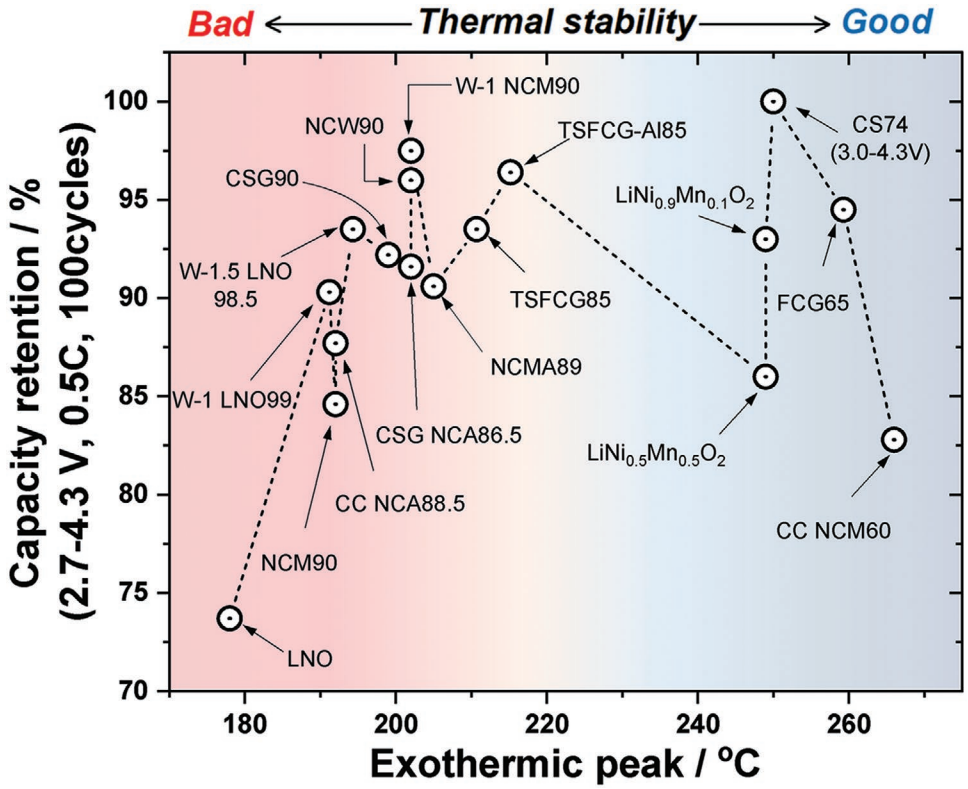

Figure 18. Comparison of the structural and thermal stabilities of the different Ni-rich cathode materials.

techniques that combine the advantages of brilliant strategies that are simultaneous yet simple should be developed for Ni-rich cathode materials with an Ni content of >90% (**Figure 20**), thus paving the way for structural and safety improvements in materials to be utilized in high-energy LIBs. The successful commercialization of Co-less Ni-rich cathodes for high-energy density batteries for EV applications is an important task in the coming years. Ni-rich cathodes with decreased amount of Co and increased operation voltages are pushing the energy densities to 350 Wh kg^{-1} and the driving distance to 600 km per

Table 4. Summary of Ni-rich cathode materials and their electrochemical and thermal properties.

Materials	Contents	Exothermic peak [°C]	Heat generation [J g^{-1}]	Voltage [V]	Initial capacity [mAh g^{-1}]	Capacity retention	Energy density	Ref.
$LiNiO_2$	LNO	178	1827	2.7–4.3 V	247.5	73.7% at 0.5 C	940.5	[25]
$LiNi_{0.99}W_{0.01}O_2$	W-1 LNO	191.2	1309	2.7–4.3 V	242.7	90.3% at 0.5 C	917.406	[42]
$Li[Ni_{0.885}Co_{0.100}Al_{0.015}]O_2$	CC NCA	192	1789	2.7–4.3 V	225	84.6% at 0.5 C	843.75	[142]
$Li[Ni_{0.90}Co_{0.05}Mn_{0.05}]O_2$	NCM90	192	1561	2.7–4.3 V	225	87.7% at 0.5 C	855	[97]
$LiNi_{0.985}W_{0.015}O_2$	W-1.5 LNO	194.3	1235	2.7–4.3 V	236.1	93.5% at 0.5 C	883.014	[42]
$Li[Ni_{0.9}Co_{0.05}Mn_{0.05}]O_2$	CSG90	199	–	2.7–4.3 V	228.7	92.2% at 0.5 C	869.06	[110]
$Li[Ni_{0.865}Co_{0.120}Al_{0.015}]O_2$	CSG NCA	202	1409	2.7–4.3 V	222	91.6% at 0.5 C	832.5	[142]
$Li[Ni_{0.9}Co_{0.09}W_{0.01}]O_2$	NCW90	202	1261	2.7–4.3 V	231.2	96% at 0.5 C	867	[95]
$Li[Ni_{0.896}Co_{0.047}Mn_{0.047}W_{0.010}]O_2$	W1.0-NCM90	202	–	2.7–4.3 V	225	97.5% at 0.5 C	855	[98]
$Li[Ni_{0.89}Co_{0.05}Mn_{0.05}Al_{0.01}]O_2$	NCMA89	205	1384	2.7–4.3 V	228	90.6% at 0.5 C	866.4	[97]
$Li[Ni_{0.85}Co_{0.05}Mn_{0.10}]O_2$	TSFCG85	210.7	–	2.7–4.3 V	222	93.5% at 0.5 C	843.6	[107]
$Li[Ni_{0.84}Co_{0.06}Mn_{0.09}Al_{0.01}]O_2$	TSFCG–Al	215.2	–	2.7–4.3 V	221	96.4% at 0.5 C	839.8	[111]
$LiNi_{0.5}Mn_{0.5}O_2$	–	249	485.7	2.7–4.3 V	163.5	86% at 0.5 C	621.3	[32]
$LiNi_{0.9}Mn_{0.1}O_2$	–	249	794.6	2.7–4.3 V	212.3	93% at 0.5 C	806.74	
$Li[(Ni_{0.8}Co_{0.1}Mn_{0.1})_{0.8}(Ni_{0.5}Mn_{0.5})_{0.2}]O_2$	CS	250	–	3.0–4.3 V	180	100% at 0.5 C	684	[143]
$Li[Ni_{0.60}Co_{0.15}Mn_{0.25}]O_2$	FCG65	259.3	–	2.7–4.3 V	194	94.5% at 0.5 C	727.5	[107]
$Li[Ni_{0.60}Co_{0.15}Mn_{0.25}]O_2$	CC NCM	266	–	2.7–4.5 V	194	82.8% at 0.5 C	737.2	[106]
$Li[Ni_{0.886}Co_{0.049}Mn_{0.050}Al_{0.015}]O_2$	NCA–NCMA	–	–	2.7–4.3 V	215	96.1% at 0.5 C	817	[113]

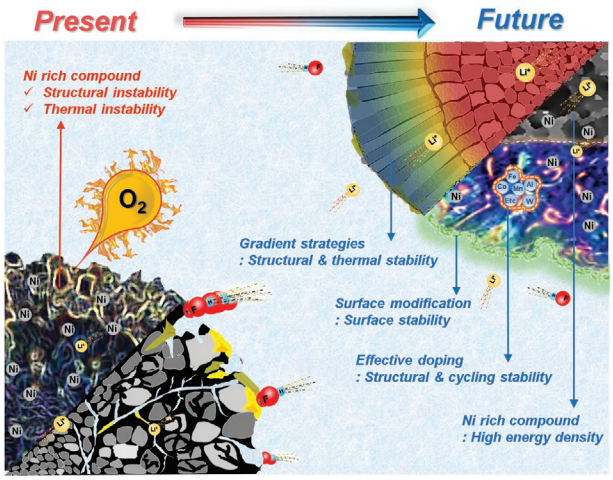

Figure 19. Schematic illustration of the surface and structural chemistries of present $LiNiO_2$ and future $LiNiO_2$ with advanced strategies such as effective doping, surface modification, and compositional and structural design.

charge. Commercialization of these cathodes has so far been proven to be difficult because of a few major challenges, and further innovations to eliminate these issues are paramount. Indeed, Ni-rich materials require more complex production and handling processes than LCO and other Ni-poor layered materials. The Co-precipitation method with strictly adjusted parameters, calcination in O_2 gas flow, and postsynthesis surface treatments are the most important production steps. There is no doubt that a key parameter is upscaling and optimization of robust high purity nickel hydroxide production methods that include dopants or process via elemental concentration gradient technology. Post electro-/ionic-conducting surface treatments of Co-less Ni-rich cathode materials would be essential procedures to compensate the energy penalty originating from the electro-inactive dopants, because rationally designed surface layers provide pivotal roles to minimize not only side

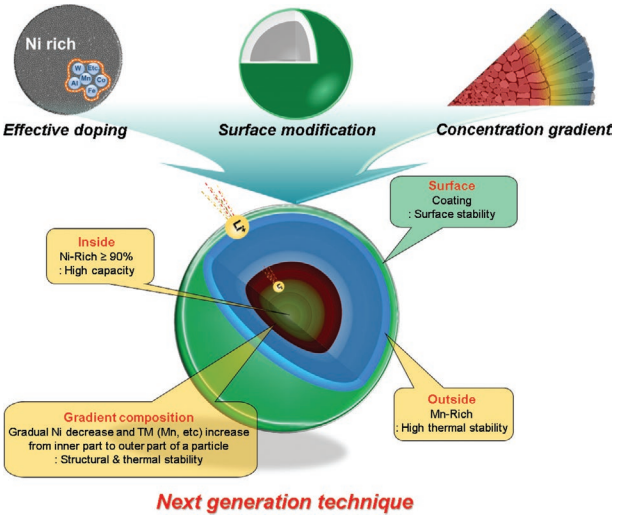

Figure 20. Schematic illustration of next generation technique for Ni rich cathode materials with over 90% Ni content, which is simple and simultaneous method.

effects occurred at electrode/electrolyte interface. Therefore, the optimized bulk and surface structures can boost the electrode performance and safety. Increasing the electrode density and loading level of Ni-rich cathodes are other important requisites for improving the volumetric energy density of LIBs. Therefore, the Ni-rich cathode materials require further efficiency improvements, and the production needs to ensure cost competitiveness with the currently used state-of-the-art NCA and NCM cathode materials. The above-mentioned would be the final destination that maximizes the possibility of commercialization for Ni rich cathode materials with over 90% Ni content to ensure future Ni-rich materials that are superior to currently used state-of-the-art NCA and NCM cathodes in all aspects.

Acknowledgements

This research was supported by the Basic Science Research Program through the National Research Foundation of Korea (NRF-2015M3D1A1069713, NRF-2019H1D8A2106002, 2020R1A2B5B01095954, and NRF-2020R1A6A1A03043435) and by a Human Resources Development programme (No. 20184010201720) of a Korea Institute of Energy Technology Evaluation and Planning (KETEP) grant, funded by the Ministry of Trade, Industry and Energy of the Korean government.

Conflict of Interest

The authors declare no conflict of interest.

Keywords

batteries, Co-less Ni-rich cathodes, layered oxides, lithium, Li-ion batteries

Received: June 22, 2020
Revised: August 25, 2020
Published online: September 27, 2020

[1] M. S. Whittingham, *Science* **1976**, *192*, 1126.
[2] K. Mizushima, P. C. Jones, P. J. Wiseman, J. B. Goodenough, *Mater. Res. Bull.* **1980**, *15*, 783.
[3] R. Yazami, P. Touzain, *J. Power Sources* **1983**, *9*, 365.
[4] J. M. Tarascon, E. Wang, F. K. Shokoohi, W. R. McKinnon, S. Colson, *J. Electrochem. Soc.* **1991**, *138*, 2859.
[5] a) F. Schipper, D. Aurbach, *R. J. Electrochem.* **2016**, *52*, 1095; b) S.-T. Myung, K. Amine, Y.-K. Sun, *J. Power Sources* **2015**, *283*, 219; c) W. Liu, P. Oh, X. Liu, M.-J. Lee, W. Cho, S. Chae, Y. Kim, J. Cho, *Angew. Chem., Int. Ed.* **2015**, *54*, 4440; d) B. Dunn, H. Kamath, J.-M. Tarascon, *Science* **2011**, *334*, 928; e) J. B. Goodenough, K.-S. Park, *J. Am. Chem. Soc.* **2013**, *135*, 1167.
[6] a) W. Li, E. Erickson, A. Manthiram, *Nat. Energy* **2011**, *108*, 80; b) K. Karthikeyan, S. Amaresh, G. W. Lee, V. Aravindan, H. Kim, K. S. Kang, W. S. Kim, Y. S. Lee, *Electrochim. Acta* **2012**, *68*, 246; c) L. Liu, M. Li, L. Chu, B. Jiang, L. Ruoxu, Z. Xiopei, G. Cao, *Prog. Mater. Sci.* **2020**, *5*, 1136.
[7] J. R. Dahn, U. von Sacken, C. A. Michal, *Solid State Ionics* **1990**, *44*, 87.
[8] A. Manthiram, A. Vadivel Murugan, A. Sarkar, T. Muraliganth, *Energy Environ. Sci.* **2008**, *1*, 621.

[9] a) F. Lin, I. M. Markus, D. Nordlund, T.-C. Weng, M. D. Asta, H. L. Xin, M. M. Doeff, *Nat. Comm.* **2014**, *5*, 3529; b) Y. Hinuma, Y. S. Meng, K. Kang, G. Ceder, *Chem. Mater.* **2007**, *19*, 1790.
[10] K. Hirakawa, H. Kadowaki, K. Ubukoshi, *J. Phys. Soc. Jpn.* **1985**, *54*, 3526.
[11] L. Wang, T. Maxisch, G. Ceder, *Chem. Mater.* **2007**, *19*, 543.
[12] a) H. Liu, M. Wolf, K. Karki, Y.-S. Yu, E. A. Stach, J. Cabana, K. W. Chapman, P. J. Chupas, *Nano Lett.* **2017**, *17*, 3452; b) Y.-N. Zhou, J. Ma, E. Hu, X. Yu, L. Gu, K.-W. Nam, L. Chen, Z. Wang, X.-Q. Yang, *Nat. Commun.* **2014**, *5*, 5381.
[13] S. Watanabe, M. Kinoshita, T. Hosokawa, K. Morigaki, K. Nakura, *J. Power Sources* **2014**, *260*, 50.
[14] F. Schipper, E. M. Erickson, C. Erk, J.-Y. Shin, F. F. Chesneau, D. Aurbach, *J. Electrochem. Soc.* **2017**, *164*, A6220.
[15] A. W. Moses, H. G. G. Flores, J.-G. Kim, M. A. Langell, *Appl. Surf. Sci.* **2007**, *253*, 4782.
[16] C. Delmas, L. Croguennec, *MRS Bull.* **2002**, *27*, 608.
[17] P. Kalyani, N. Kalaiselvi, *Sci. Technol. Adv. Mater.* **2005**, *6*, 689.
[18] Y. S. Lee, Y. K. Sun, K. S. Nahm, *Solid State Ionics* **1999**, *118*, 159.
[19] L. D. Dyer, B. S. Borie, G. P. Smith, *J. Am. Chem. Soc.* **1954**, *76*, 1499.
[20] T. Ohzuku, A. Ueda, M. Nagayama, *J. Electrochem. Soc.* **1993**, *140*, 1862.
[21] T. Ohzuku, *J. Electrochem. Soc.* **1993**, *140*, 1862.
[22] a) S.-K. Hu, G.-H. Cheng, M.-Y. Cheng, B.-J. Hwang, R. Santhanam, *J. Power Sources* **2009**, *188*, 564; b) Y.-M. Choi, S.-I. Pyun, S.-I. Moon, *Solid State Ionics* **1996**, *89*, 43; c) J. Morales, C. Pérez-Vicente, J. L. Tirado, *Mater. Res. Bull.* **1990**, *25*, 623.
[23] A. Rougier, P. Gravereau, C. Delmas, *J. Electrochem. Soc.* **1996**, *143*, 1168.
[24] C. Delmas, M. Ménétrier, L. Croguennec, S. Levasseur, J. P. Pérès, C. Pouillerie, G. Prado, L. Fournès, F. Weill, *Int. J. Inorg. Mater.* **1999**, *1*, 11.
[25] C. S. Yoon, D.-W. Jun, S.-T. Myung, Y.-K. Sun, *ACS Energy Lett.* **2017**, *2*, 1150.
[26] C. S. Yoon, H.-H. Ryu, G.-T. Park, J.-H. Kim, K.-H. Kim, Y.-K. Sun, *J. Mater. Chem. A* **2018**, *6*, 4126.
[27] L. Croguennec, C. Pouillerie, C. Delmas, *J. Electrochem. Soc.* **2000**, *147*, 1314.
[28] L. de Biasi, A. Schiele, M. Roca-Ayats, G. Garcia, T. Brezesinski, P. Hartmann, J. Janek, *ChemSusChem* **2019**, *12*, 2240.
[29] F. Kong, C. Liang, L. Wang, Y. Zheng, S. Perananthan, R. C. Longo, J. P. Ferraris, M. Kim, K. Cho, *Adv. Energy Mater.* **2019**, *9*, 1802586.
[30] K.-K. Lee, W.-S. Yoon, K.-B. Kim, K.-Y. Lee, S.-T. Hong, *J. Power Sources* **2001**, *97*, 321.
[31] C. Pouillerie, L. Croguennec, P. Biensan, P. Willmann, C. Delmas, *J. Electrochem. Soc.* **2000**, *147*, 2061.
[32] Y.-K. Sun, D.-J. Lee, Y. J. Lee, Z. Chen, S.-T. Myung, *ACS Appl. Mater. Interfaces* **2013**, *5*, 11434.
[33] a) P. Mohan, K. A. Kumar, G. P. Kalaignan, V. S. Muralidharan, *J. Solid State Electrochem.* **2012**, *16*, 3695; b) V. R. Galakhov, E. Z. Kurmaev, S. Uhlenbrock, M. Neumann, D. G. Kellerman, V. S. Gorshkov, *Solid State Commun.* **1995**, *95*, 347.
[34] F. Nobili, F. Croce, B. Scrosati, R. Marassi, *Chem. Mater.* **2001**, *13*, 1642.
[35] B. J. Hwang, R. Santhanam, C. H. Chen, *J. Power Sources* **2003**, *114*, 244.
[36] P. Mohan, G. P. Kalaignan, *J. Electroceram.* **2013**, *31*, 210.
[37] M. Guilmard, A. Rougier, M. Grüne, L. Croguennec, C. Delmas, *J. Power Sources* **2003**, *115*, 305.
[38] Y. Nishida, K. Nakane, T. Satoh, *J. Power Sources* **1997**, *68*, 561.
[39] C. S. Yoon, M.-J. Choi, D.-W. Jun, Q. Zhang, P. Kaghazchi, K.-H. Kim, Y.-K. Sun, *Chem. Mater.* **2018**, *30*, 1808.
[40] J. Kim, K. Amine, *Electrochem. Commun.* **2001**, *3*, 52.
[41] P. Cui, Z. Jia, L. Li, T. He, *J. Phys. Chem. Solids* **2011**, *72*, 899.
[42] H.-H. Ryu, G.-T. Park, C. S. Yoon, Y.-K. Sun, *J. Mater. Chem. A* **2019**, *7*, 18580.
[43] R. Sathiyamoorthi, P. Shakkthivel, S. Ramalakshmi, Y.-G. Shul, *J. Power Sources* **2007**, *171*, 922.
[44] M. Guilmard, L. Croguennec, C. Delmas, *J. Electrochem. Soc.* **2003**, *150*, A1287.
[45] L. Zhang, H. Noguchi, M. Yoshio, *J. Power Sources* **2002**, *110*, 57.
[46] I. Saadoune, C. Delmas, *J. Solid State Chem.* **1998**, *136*, 8.
[47] E. Zhecheva, R. Stoyanova, *Solid State Ionics* **1993**, *66*, 143.
[48] J. Cho, G. Kim, H. S. Lim, *J. Electrochem. Soc.* **1999**, *146*, 3571.
[49] W. Li, J. N. Reimers, J. R. Dahn, *Solid State Ionics* **1993**, *67*, 123.
[50] a) C. Delmas, I. Saadoune, *Solid State Ionics* **1992**, *53–56*, 370; b) C. Delmas, I. Saadoune, A. Rougier, *J. Power Sources* **1993**, *44*, 595.
[51] a) J. U. Choi, Y. J. Park, J. H. Jo, L.-Y. Kuo, P. Kaghazchi, S.-T. Myung, *ACS Appl. Mater. Interfaces* **2018**, *10*, 40978; b) F. Wu, G.-T. Kim, M. Kuenzel, H. Zhang, J. Asenbauer, D. Geiger, U. Kaiser, S. Passerini, *Adv. Energy Mater.* **2019**, *9*, 1902445.
[52] M. Song, I. Kwon, S. Shim, J. H. Song, *Ceram. Int.* **2010**, *36*, 1225.
[53] M. K. Aydinol, A. F. Kohan, G. Ceder, *J. Power Sources* **1997**, *68*, 664.
[54] a) A. Gupta, W. D. Chemelewski, C. Buddie Mullins, J. B. Goodenough, *Adv. Mater.* **2015**, *27*, 6063; b) Z. Liu, H. Zhen, Y. Kim, C. Liang, *J. Power Sources* **2011**, *196*, 10201; c) S.-P. Lin, K.-Z. Fung, Y.-M. Hon, M.-H. Hon, *J. Solid State Chem.* **2002**, *167*, 97; d) J. U. Choi, C. S. Yoon, Q. Zhang, P. Kaghazchi, Y. H. Jung, K.-S. Lee, D.-C. Ahn, Y.-K. Sun, S.-T. Myung, *J. Mater. Chem. A* **2019**, *7*, 202.
[55] A. Aishova, G.-T. Park, C. S. Yoon, Y.-K. Sun, *Adv. Energy Mater.* **2020**, *10*, 1903179.
[56] S.-T. Myung, S. Komaba, K. Kurihara, K. Hosoya, N. Kumagai, Y.-K. Sun, I. Nakai, M. Yonemura, T. Kamiyama, *Chem. Mater.* **2006**, *18*, 1658.
[57] Z. Liu, H. Zheng, L. Tan, S. Yuan, H. Yin, *Energy Technol.* **2018**, *6*, 1302.
[58] Y.-R. Luo, J. A. Kerr, *CRC Handb. Chem.Phys.* **2012**, *89*, 89.
[59] G. Yang, E. Zhao, M. Chen, Y. Cheng, L. Xue, Z. Hu, X. Xiao, F. Li, *J. Solid State Electrochem.* **2017**, *21*, 3195.
[60] R. Stoyanova, E. Zhecheva, R. Alcántara, J. L. Tirado, *J. Mater. Chem.* **2006**, *16*, 359.
[61] D. Li, Y. Sasaki, K. Kobayakawa, Y. Sato, *Electrochim. Acta* **2006**, *51*, 3809.
[62] B. Zhang, G. Chen, P. Xu, C. C. Li, *J. Power Sources* **2008**, *176*, 325.
[63] a) Y. L. Wang, X. Huang, F. Li, J. S. Cao, S. H. Ye, *RSC Adv.* **2015**, *5*, 49651; b) V. Dávila, E. Lima, S. Bulbulian, P. Bosch, *Microporous Mesoporous Mater.* **2008**, *107*, 240.
[64] a) S.-T. Myung, S. Komaba, K. Hosoya, N. Hirosaki, Y. Miura, N. Kumagai, *Chem. Mater.* **2005**, *17*, 2427; b) Y. J. Park, J. U. Choi, J. H. Jo, C.-H. Jo, J. Kim, S.-T. Myung, *Adv. Funct. Mater.* **2019**, *29*, 1901912; c) O. Kubaschewski, *Ber. Bunsengesellsch. Phys. Chem.* **1982**, *86*, 761.
[65] M. Guilmard, L. Croguennec, D. Denux, C. Delmas, *Chem. Mater.* **2003**, *15*, 4476.
[66] J. Cho, H. Jung, Y. Park, G. Kim, H. S. Lim, *J. Electrochem. Soc.* **2000**, *147*, 15.
[67] a) J. Li, L. E. Downie, L. Ma, W. Qiu, J. R. Dahn, *J. Electrochem. Soc.* **2015**, *162*, A1401; b) J.-L. Shi, D.-D. Xiao, M. Ge, X. Yu, Y. Chu, X. Huang, X.-D. Zhang, Y.-X. Yin, X.-Q. Yang, Y.-G. Guo, L. Gu, L.-J. Wan, *Adv. Mater.* **2018**, *30*, 1705575.
[68] W. Lee, S. Muhammad, T. Kim, H. Kim, E. Lee, M. Jeong, S. Son, J.-H. Ryou, W.-S. Yoon, *Adv. Energy Mater.* **2018**, *8*, 1870015.
[69] H.-J. Noh, S. Youn, C. S. Yoon, Y.-K. Sun, *J. Power Sources* **2013**, *233*, 121.
[70] G. W. Nam, N.-Y. Park, K.-J. Park, J. Yang, J. Liu, C. S. Yoon, Y.-K. Sun, *ACS Energy Lett.* **2019**, *4*, 2995.
[71] W. Yang, W. Xiang, Y.-X. Chen, Z.-G. Wu, W.-B. Hua, L. Qiu, F.-R. He, J. Zhang, B.-H. Zhong, X.-D. Guo, *ACS Appl. Mater. Interfaces* **2020**, *12*, 10240.

[72] W. Lee, S. Muhammad, T. Kim, H. Kim, E. Lee, M. Jeong, S. Son, J.-H. Ryou, W.-S. Yoon, *Adv. Energy Mater.* **2018**, *8*, 1701788.
[73] S. Hwang, W. Chang, S. M. Kim, D. Su, D. H. Kim, J. Y. Lee, K. Y. Chung, E. A. Stach, *Chem. Mater.* **2014**, *26*, 1084.
[74] J.-H. Kim, K.-J. Park, S. J. Kim, C. S. Yoon, Y.-K. Sun, *J. Mater. Chem. A* **2019**, *7*, 2694.
[75] S.-M. Bak, E. Hu, Y. Zhou, X. Yu, S. D. Senanayake, S.-J. Cho, K.-B. Kim, K. Y. Chung, X.-Q. Yang, K.-W. Nam, *ACS Appl. Mater. Interfaces* **2014**, *6*, 22594.
[76] K.-W. Nam, S.-M. Bak, E. Hu, X. Yu, Y. Zhou, X. Wang, L. Wu, Y. Zhu, K.-Y. Chung, X.-Q. Yang, *Adv. Funct. Mater.* **2013**, *23*, 1047.
[77] S.-T. Myung, K.-S. Lee, C. S. Yoon, Y.-K. Sun, K. Amine, H. Yashiro, *J. Phys. Chem. C* **2010**, *114*, 4710.
[78] D.-H. Cho, C.-H. Jo, W. Cho, Y.-J. Kim, H. Yashiro, Y.-K. Sun, S.-T. Myung, *J. Electrochem. Soc.* **2014**, *161*, A920.
[79] P. Oh, M. Ko, S. Myeong, Y. Kim, J. Cho, *Adv. Energy Mater.* **2014**, *4*, 1400631.
[80] A. M. Wise, C. Ban, J. N. Weker, S. Misra, A. S. Cavanagh, Z. Wu, Z. Li, M. S. Whittingham, K. Xu, S. M. George, M. F. Toney, *Chem. Mater.* **2015**, *27*, 6146.
[81] S.-T. Myung, K. Izumi, S. Komaba, Y.-K. Sun, H. Yashiro, N. Kumagai, *Chem. Mater.* **2005**, *17*, 3695.
[82] C.-H. Jo, D.-H. Cho, H.-J. Noh, H. Yashiro, Y.-K. Sun, S. T. Myung, *Nano Res.* **2015**, *8*, 1464.
[83] J. Kim, H. Ma, H. Cha, H. Lee, J. Sung, M. Seo, P. Oh, M. Park, J. Cho, *Energy Environ. Sci.* **2018**, *11*, 1449.
[84] J. H. Jo, C.-H. Jo, H. Yashiro, S.-J. Kim, S.-T. Myung, *J. Power Sources* **2016**, *313*, 1.
[85] H. Yang, H.-H. Wu, M. Ge, L. Li, Y. Yuan, Q. Yao, J. Chen, L. Xia, J. Zheng, Z. Chen, J. Duan, K. Kisslinger, X. C. Zeng, W.-K. Lee, Q. Zhang, J. Lu, *Adv. Funct. Mater.* **2019**, *29*, 1808825.
[86] J. W. Kim, J. J. Travis, E. Hu, K.-W. Nam, S. C. Kim, C. S. Kang, J.-H. Woo, X.-Q. Yang, S. M. George, K. H. Oh, S.-J. Cho, S.-H. Lee, *J. Power Sources* **2014**, *254*, 190.
[87] H. Li, M. Cormier, N. Zhang, J. Inglis, J. Li, J. R. Dahn, *J. Electrochem. Soc.* **2019**, *166*, A429.
[88] H.-H. Sun, A. Manthiram, *Chem. Mater.* **2017**, *29*, 8486.
[89] C. S. Yoon, M. H. Choi, B.-B. Lim, E.-J. Lee, Y.-K. Sun, *J. Electrochem. Soc.* **2015**, *162*, A2483.
[90] K.-J. Park, J.-Y. Hwang, H.-H. Ryu, F. Maglia, S.-J. Kim, P. Lamp, C. S. Yoon, Y.-K. Sun, *ACS Energy Lett.* **2019**, *4*, 1394.
[91] a) X. Yang, J. Chen, Q. Zheng, W. Tu, L. Xing, Y. Liao, M. Xu, Q. Huang, G. Cao, W. Li, *J. Mater. Chem. A* **2018**, *6*, 16149; b) L. Zhang, J. Fu, C. Zhang, *Nanoscale Res Lett.* **2017**, *12*, 376; c) S. Watanabe, M. Kinoshita, T. Hosokawa, K. Morigaki, K. Nakura, *J. Power Sources* **2014**, *258*, 210.
[92] a) Y. Kim, D. Kim, *ACS Appl. Mater. Interfaces* **2012**, *4*, 586; b) H. Xie, K. Du, G. Hu, J. Duan, Z. Peng, Z. Zhang, Y. Cao, *J. Mater. Chem. A* **2015**, *3*, 20236.
[93] M. Guilmard, C. Pouillerie, L. Croguennec, C. Delmas, *Solid State Ionics* **2003**, *160*, 39.
[94] J. Xu, F. Lin, M. M. Doeff, W. Tong, *J. Mater. Chem. A* **2017**, *5*, 874.
[95] H.-H. Ryu, K.-J. Park, D. R. Yoon, A. Aishova, C. S. Yoon, Y.-K. Sun, *Adv. Energy Mater.* **2019**, *9*, 1970174.
[96] W. Li, S. Lee, A. Manthiram, *Adv. Mater.* **2020**, *32*, 2002718.
[97] U.-H. Kim, L.-Y. Kuo, P. Kaghazchi, C. S. Yoon, Y.-K. Sun, *ACS Energy Lett.* **2019**, *4*, 576.
[98] G.-T. Park, H.-H. Ryu, N.-Y. Park, C. S. Yoon, Y.-K. Sun, *J. Power Sources* **2019**, *442*, 227242.
[99] R. Zhao, Z. Yang, J. Liang, D. Lu, C. Liang, X. Guan, A. Gao, H. Chen, *J. Alloys. Compd.* **2016**, *689*, 318.
[100] Z. Huang, Z. Wang, X. Zheng, H. Guo, X. Li, Q. Jing, Z. Yang, *RSC Adv.* **2015**, *5*, 88773.
[101] Q.-X. Du, Z.-F. Tang, X.-H. Ma, Y. Zang, X. Sun, Y. Shao, Z.-Y. Wen, C.-H. Chen, *Solid State Ionics* **2015**, *279*, 11.
[102] M. Dixit, B. Markovsky, D. Aurbach, D. T. Major, *J. Electrochem. Soc.* **2017**, *164*, A6359.
[103] D. Aurbach, O. Srur-Lavi, C. Ghanty, M. Dixit, O. Haik, M. Talianker, Y. Grinblat, N. Leifer, R. Lavi, D. T. Major, G. Goobes, E. Zinigrad, E. M. Erickson, M. Kosa, B. Markovsky, J. Lampert, A. Volkov, J.-Y. Shin, A. Garsuch, *J. Electrochem. Soc.* **2015**, *162*, A1014.
[104] Y.-K. Sun, S.-T. Myung, M.-H. Kim, J.-H. Kim, *Electrochem. Solid State Lett.* **2006**, *9*, A171.
[105] Y.-K. Sun, S.-T. Myung, B.-C. Park, J. Prakash, I. Belharouak, K. Amine, *Nat. Mater.* **2009**, *8*, 320.
[106] H.-J. Noh, Z. Chen, C. S. Yoon, J. Lu, K. Amine, Y.-K. Sun, *Chem. Mater.* **2013**, *25*, 2109.
[107] C. S. Yoon, K.-J. Park, U.-H. Kim, K. H. Kang, H.-H. Ryu, Y.-K. Sun, *Chem. Mater.* **2017**, *29*, 10436.
[108] D.-W. Jun, C. S. Yoon, U.-H. Kim, Y.-K. Sun, *Chem. Mater.* **2017**, *29*, 5048.
[109] a) B. C. Park, H. J. Bang, K. Amine, E. Jung, Y. K. Sun, *J. Power Sources* **2007**, *174*, 658; b) K.-S. Lee, S.-T. Myung, Y.-K. Sun, *J. Power Sources* **2010**, *195*, 6043.
[110] U.-H. Kim, H.-H. Ryu, J.-H. Kim, R. Mücke, P. Kaghazchi, C. S. Yoon, Y.-K. Sun, *Adv. Energy Mater.* **2019**, *9*, 1803902.
[111] B.-B. Lim, S.-T. Myung, C. S. Yoon, Y.-K. Sun, *ACS Energy Lett.* **2016**, *1*, 283.
[112] B.-B. Lim, S.-J. Yoon, K.-J. Park, C. S. Yoon, S.-J. Kim, J. J. Lee, Y.-K. Sun, *Adv. Funct. Mater.* **2015**, *25*, 4673.
[113] U.-H. Kim, J.-H. Kim, J.-Y. Hwang, H.-H. Ryu, C. S. Yoon, Y.-K. Sun, *Mater. Today* **2019**, *23*, 26.
[114] C. Xu, W. Xiang, Z. Wu, Y. Xu, Y. Li, Y. Wang, Y. Xiao, X. Guo, B. Zhong, *ACS Appl. Mater. Interfaces* **2019**, *11*, 16629.
[115] Y.-K. Sun, Z. Chen, H.-J. Noh, D.-J. Lee, H.-G. Jung, Y. Ren, S. Wang, C. S. Yoon, S.-T. Myung, K. Amine, *Nat. Mater.* **2012**, *11*, 942.
[116] U.-H. Kim, E.-J. Lee, C. S. Yoon, S.-T. Myung, Y.-K. Sun, *Adv. Energy Mater.* **2016**, *6*, 1601417.
[117] M. R. Laskar, D. H. K. Jackson, Y. Guan, S. Xu, S. Fang, M. Dreibelbis, M. K. Mahanthappa, D. Morgan, R. J. Hamers, T. F. Kuech, *ACS Appl. Mater. Interfaces* **2016**, *8*, 10572.
[118] J.-Z. Kong, C. Ren, G.-A. Tai, X. Zhang, A.-D. Li, D. Wu, H. Li, F. Zhou, *J. Power Sources* **2014**, *266*, 433.
[119] W. Zhu, X. Huang, T. Liu, Z. Xie, Y. Wang, K. Tian, L. Bu, H. Wang, L. Gao, J. Zhao, *Coatings* **2019**, *9*, 92.
[120] S. Neudeck, A. Mazilkin, C. Reitz, P. Hartmann, J. Janek, T. Brezesinski, *Sci. Rep.* **2019**, *9*, 5328.
[121] M. R. Laskar, D. H. K. Jackson, S. Xu, R. J. Hamers, D. Morgan, T. F. Kuech, *ACS Appl. Mater. Interfaces* **2017**, *9*, 11231.
[122] C. Qin, J. Cao, J. Chen, G. Dai, T. Wu, Y. Chen, Y. Tang, A. Li, Y. Chen, *Dalton Trans.* **2016**, *45*, 9669.
[123] G. Dai, H. Du, S. Wang, J. Cao, M. Yu, Y. Chen, Y. Tang, A. Li, Y. Chen, *RSC Adv.* **2016**, *6*, 100841.
[124] M. L. Marcinek, J. W. Wilcox, M. M. Doeff, R. M. Kostecki, *J. Electrochem. Soc.* **2009**, *156*, A48.
[125] S. J. Shi, J. P. Tu, Y. Y. Tang, Y. Q. Zhang, X. Y. Liu, X. L. Wang, C. D. Gu, *J. Power Sources* **2013**, *225*, 338.
[126] M. Zhang, G. Hu, L. Liang, Z. Peng, K. Du, Y. Cao, *J. Alloys Compd.* **2016**, *673*, 237.
[127] Z.-F. Tang, R. Wu, P.-F. Huang, Q.-S. Wang, C.-H. Chen, *J. Alloys Compd.* **2017**, *693*, 1157.
[128] K. Meng, Z. Wang, H. Guo, X. Li, D. Wang, *Electrochim. Acta* **2016**, *211*, 822.
[129] Y. Chen, Y. Zhang, B. Chen, Z. Wang, C. Lu, *J. Power Sources* **2014**, *256*, 20.
[130] S. Li, X. Fu, J. Zhou, Y. Han, P. Qi, X. Gao, X. Feng, B. Wang, *J. Mater. Chem. A* **2016**, *4*, 5823.
[131] S. Liu, H. Wu, L. Huang, M. Xiang, H. Liu, Y. Zhang, *J. Alloys Compd.* **2016**, *674*, 447.

[132] S. Guo, B. Yuan, H. Zhao, D. Hua, Y. Shen, C. Sun, T. Chen, W. Sun, J. Wu, B. Zheng, W. Zhang, S. Li, F. Huo, *Nano Energy* **2019**, *58*, 673.
[133] K. Yang, L.-Z. Fan, J. Guo, X. Qu, *Electrochim. Acta* **2012**, *63*, 363.
[134] S. Chen, T. He, Y. Su, Y. Lu, L. Bao, L. Chen, Q. Zhang, J. Wang, R. Chen, F. Wu, *ACS Appl. Mater. Interfaces* **2017**, *9*, 29732.
[135] R. Zhao, J. Liang, J. Huang, R. Zeng, J. Zhang, H. Chen, G. Shi, *J. Alloys Compd.* **2017**, *724*, 1109.
[136] L. Li, Z. Chen, Q. Zhang, M. Xu, X. Zhou, H. Zhu, K. Zhang, *J. Mater. Chem. A* **2015**, *3*, 894.
[137] W. Liu, X. Li, D. Xiong, Y. Hao, J. Li, H. Kou, B. Yan, D. Li, S. Lu, A. Koo, K. Adair, X. Sun, *Nano Energy* **2018**, *44*, 111.
[138] S. Ito, S. Fujiki, T. Yamada, Y. Aihara, Y. Park, T. Y. Kim, S.-W. Baek, J.-M. Lee, S. Doo, N. Machida, *J. Power Sources* **2014**, *248*, 943.
[139] P. Zou, Z. Lin, M. Fan, F. Wang, Y. Liu, X. Xiong, *Appl. Surf. Sci.* **2020**, *504*, 144506.
[140] S.-W. Lee, M.-S. Kim, J. H. Jeong, D.-H. Kim, K. Y. Chung, K. C. Roh, K.-B. Kim, *J. Power Sources* **2017**, *360*, 206.
[141] D. Becker, M. Börner, R. Nölle, M. Diehl, S. Klein, U. Rodehorst, R. Schmuch, M. Winter, T. Placke, *ACS Appl. Mater. Interfaces* **2019**, *11*, 18404.
[142] K.-J. Park, M.-J. Choi, F. Maglia, S.-J. Kim, K.-H. Kim, C. S. Yoon, Y.-K. Sun, *Adv. Energy Mater.* **2018**, *8*, 1703612.
[143] Y.-K. Sun, S.-T. Myung, M.-H. Kim, J. Prakash, K. Amine, *J. Am. Chem. Soc.* **2005**, *127*, 13411.

Ji Ung Choi received his Ph.D. degree on cathode materials for sodium ion batteries at Sejong University under the supervision of Professor Seung-Taek Myung in 2020. He is currently a postdoctoral fellow in the group of Prof. EunAe Cho in the Department of Materials Science and Engineering at Korea Advanced Institute of Science and Technology (KAIST), Korea. He has research interests in the development of next-generation energy-storage materials and systems. His research is focused on the development of novel electrode materials for high-energy Li, Na, and K-ion batteries.

Natalia Voronina received a Ph.D. degree from Moscow State University, Russia, in 2009. After having worked at Samsung SDI from 2011 to 2014, she decided to continue her research career aiming at battery technology. She has currently been working for another Ph.D. with Professor Seung-Taek Myung in the Department of Nanotechnology and Advanced Materials Engineering at Sejong University, South Korea. Her current research interests have focused on the development of new electrode materials for lithium-ion and sodium-ion batteries.

Yang-Kook Sun received his M.S. degree and Ph.D. degree from the Seoul National University, South Korea. In 1996, he was a principal researcher at Samsung Advanced Institute of Technology and contributed to the commercialization of the lithium polymer battery. He has worked at the Hanyang University in Korea as a professor since 2000. His research covers development of new electrode materials for lithium ion batteries, sodium ion batteries, Li–S batteries, and Li–air batteries.

Seung-Taek Myung is a professor of Department of Nanotechnology and Advanced Materials Engineering at Sejong University, South Korea. Before 2011, he affiliated at VK (principal engineer), 3M (senior engineer), and Iwate University (assistant professor). He received his Ph.D. degree in Chemical Engineering from Iwate University, Japan, in 2003. His research interests embrace development of electroactive materials and corrosion of current collectors of rechargeable lithium, sodium, potassium, and zinc batteries.